(article starts on next page)

Chasing the Break: Tracing the Full Evolution of a Black Hole X-Ray Binary Jet with Multiwavelength Spectral Modeling

Constanza Echiburú-Trujillo[1,2,3] , Alexandra J. Tetarenko[4,5,6,43] , Daryl Haggard[2,3] , Thomas D. Russell[7] ,
Karri I. I. Koljonen[8,9,10] , Arash Bahramian[11] , Jingyi Wang[12] , Michael Bremer[13] , Joe Bright[14] , Piergiorgio Casella[15] ,
David M. Russell[16] , Diego Altamirano[17] , M. Cristina Baglio[18] , Tomaso Belloni[18,44] , Chiara Ceccobello[19] ,
Stephane Corbel[20] , Maria Diaz Trigo[21] , Dipankar Maitra[22] , Aldrin Gabuya[23,24] , Elena Gallo[25] , Sebastian Heinz[26] ,
Jeroen Homan[27] , Erin Kara[12] , Elmar Körding[28] , Fraser Lewis[29,30] , Matteo Lucchini[12,31,32] , Sera Markoff[31,33] ,
Simone Migliari[34] , James C. A. Miller-Jones[11] , Jerome Rodriguez[20] , Payaswini Saikia[16] , Craig L. Sarazin[35] ,
Tariq Shahbaz[36,37] , Gregory Sivakoff[38] , Roberto Soria[39,40,41] , Vincenzo Testa[15] , Bailey E. Tetarenko[2,3] , and
Valeriu Tudose[42]

[1] Department of Astrophysical and Planetary Sciences, JILA, Duane Physics Bldg., 2000 Colorado Avenue, University of Colorado, Boulder, CO 80309, USA
constanza.echiburu@colorado.edu
[2] Department of Physics, McGill University, 3600 rue University, Montreal, Québec H3A 2T8, Canada
[3] Trottier Space Institute, 3550 Rue University, Montréal, Québec H3A 2A7, Canada
[4] Department of Physics and Astronomy, University of Lethbridge, Lethbridge, Alberta T1K 3M4, Canada
[5] Department of Physics and Astronomy, Texas Tech University, Lubbock, TX 79409-1051, USA
[6] East Asian Observatory, 660 N. A'ohōkū Place, University Park, Hilo, HI 96720, USA
[7] INAF, Istituto di Astrofisica Spaziale e Fisica Cosmica, Via U. La Malfa 153, I-90146 Palermo, Italy
[8] Institutt for Fysikk, Norwegian University of Science and Technology, Høgskloreringen 5, Trondheim NO-7491, Norway
[9] Finnish Centre for Astronomy with ESO (FINCA), University of Turku, Väisäläntie 20, FI-21500 Piikkiö, Finland
[10] Aalto University, Metsahovi Radio Observatory, P.O. Box 13000, FI-00076 Aalto, Finland
[11] International Centre for Radio Astronomy Research, Curtin University, Bentley, WA 6102, Australia
[12] MIT Kavli Institute for Astrophysics and Space Research, MIT, 70 Vassar Street, Cambridge, MA 02139, USA
[13] Institut de Radioastronomie Millimétrique, 300 Rue de la Piscine, F-38406 Saint Martin d'Hères, France
[14] Astrophysics, Department of Physics, University of Oxford, Keble Road, Oxford OX1 3RH, UK
[15] INAF—Osservatorio Astronomico di Roma, Via Frascati 33, I-00078 Monteporzio Catone, Italy
[16] Center for Astrophysics and Space Science (CASS), New York University Abu Dhabi, P.O. Box 129188, Abu Dhabi, UAE
[17] School of Physics and Astronomy, University of Southampton, Southampton SO17 1BJ, UK
[18] INAF-Osservatorio Astronomico di Brera, Via Bianchi 46, I-23807 Merate (LC), Italy
[19] Department of Space, Earth and Environment, Chalmers University of Technology, Onsala Space Observatory, SE-439 92 Onsala, Sweden
[20] Université Paris-Saclay, Université Paris-Cité, CEA, CNRS, AIM, F-91191 Gif-sur-Yvette, France
[21] ESO, Karl-Schwarzschild-Strasse 2, D-85748 Garching bei München, Germany
[22] Department of Physics and Astronomy, Wheaton College, Norton, MA 02766, USA
[23] Al Sadeem Observatory, Al Wathba South, Abu Dhabi, UAE
[24] Rizal Technological University, Mandaluyong City, Philippines
[25] Department of Astronomy, University of Michigan, 1085 South University Avenue, Ann Arbor, MI 48109, USA
[26] Department of Astronomy, University of Wisconsin Madison, 475 N. Charter Street, Madison, WI 53706, USA
[27] Eureka Scientific, Inc., 2452 Delmer Street, Oakland, CA 94602, USA
[28] Department of Astrophysics/IMAPP, Radboud University, P.O. Box 9010, 6500 GL Nijmegen, The Netherlands
[29] Faulkes Telescope Project, School of Physics and Astronomy, Cardiff University, The Parade, Cardiff CF24 3AA, Wales, UK
[30] Astrophysics Research Institute, Liverpool John Moores University, 146 Brownlow Hill, Liverpool L3 5RF, UK
[31] Anton Pannekoek Institute for Astronomy, University of Amsterdam, Science Park 904, Amsterdam NL-1098 XH, The Netherlands
[32] SRON Netherlands Institute for Space Research, Niels Bohrweg 4, 2333CA Leiden, The Netherlands
[33] Gravitation Astroparticle Physics Amsterdam (GRAPPA) Institute, University of Amsterdam, Science Park NL-904, Amsterdam 1098 XH, The Netherlands
[34] Aurora Technology, Calle Principe de Vergara, 211, 1-B, E-28002 Madrid, Spain
[35] Department of Astronomy, University of Virginia, 530 McCormick Road, Charlottesville, VA 22904-4325, USA
[36] Instituto de Astrofísica de Canarias (IAC), E-38205 La Laguna, Tenerife, Spain
[37] Departamento de Astrofísica, Universidad de La Laguna (ULL), E-38206 La Laguna, Tenerife, Spain
[38] Department of Physics, University of Alberta, CCIS 4-181, Edmonton AB T6G 2E1, Canada
[39] INAF, Osservatorio Astrofisico di Torino, Strada Osservatorio 20, I-10025 Pino Torinese, Italy
[40] College of Astronomy and Space Sciences, University of the Chinese Academy of Sciences, Beijing 100049, People's Republic of China
[41] Sydney Institute for Astronomy, School of Physics A28, The University of Sydney, Sydney, NSW 2006, Australia
[42] Institute for Space Sciences, Atomistilor 409, P.O. Box MG-23, 077125 Bucharest-Magurele, Romania

Abstract

Black hole (BH) X-ray binaries (XRBs) are ideal targets to study the connection between accretion inflow and jet outflow. Here we present quasi-simultaneous, multiwavelength observations of the Galactic BH system

---

[43] Former NASA Einstein Fellow.
[44] Deceased.

MAXI J1820+070, throughout its 2018–2019 outburst. Our data set includes coverage from the radio through X-ray bands from 17 different instruments/telescopes, and encompasses 19 epochs over a 7 month period, resulting in one of the most well-sampled multiwavelength data sets of a BH XRB outburst to date. With our data, we compile and model the broadband spectra of this source using a phenomenological model that includes emission from the jet, a companion star, and an accretion flow. This modeling allows us to track the evolution of the spectral break in the jet spectrum, a key observable that samples the jet launching region. We find that the spectral break location changes over at least ≈ 3 orders of magnitude in electromagnetic frequency over this period. Using these spectral break measurements, we link the full cycle of jet behavior, including the rising, quenching, and reignition, to the changing accretion flow properties as the source evolves through its different accretion states. Our analysis shows consistent jet behavior with other sources in similar phases of their outbursts, reinforcing the idea that jet quenching and recovery may be a global feature of BH XRB systems in outburst. Our results also provide valuable evidence supporting a close connection between the geometry of the inner accretion flow and the base of the jet.

Unified Astronomy Thesaurus concepts: X-ray binary stars (1811); Low-mass x-ray binary stars (939); Radio jets (1347)

Supporting material: machine-readable tables

1. Introduction

Black hole (BH) X-ray binaries (XRBs) consist of a stellar-mass BH accreting material from a companion star. Since this accreted material carries angular momentum, it forms an accretion disk around the BH, where some of the material can be transported away from the disk in the form of a relativistic plasma jet (Fender 2006). The physical processes involved in jet launching are still a matter of debate, as are the composition of the jet material and the amount of energy carried away from the system. However, the launching mechanism is thought to be connected to the accretion process, suggesting a close relationship between the emission properties of the disk and the jet in these systems (e.g., Fender et al. 2004; Miller-Jones et al. 2012; Russell et al. 2014, 2020b; Koljonen et al. 2015; Wood et al. 2021). Thanks to their close distances of order kiloparsecs (see Jonker & Nelemans 2004; Tetarenko et al. 2016, and references therein), and because they present variability on timescales ranging from hours to a few days, BH XRBs are ideal systems to track changes in the accretion inflow and jet outflow in real time as the sources evolve through different accretion states, and therefore provide insight into the disk–jet connection.

The different accretion states observed in BH XRBs during a typical outburst are marked by changes in the structure of the accretion flow (Homan & Belloni 2005; Belloni et al. 2011). At low mass accretion rates, the system is in the hard state, where the inner accretion flow is hot, optically thin, and geometrically thick (although still debated, this is known as the corona). The hard state is associated with the presence of a compact jet, a continuous and highly collimated outflow with opening angle $< 10°$ (Miller-Jones et al. 2006) and Lorentz factor $= 1.3–3.5$ (Saikia et al. 2019) detected in the radio bands. As the accretion rate increases, the system moves from the hard state into the soft state, a transition state known as the hard intermediate state (HIMS). During this process, jets are observed to take the form of discrete clouds of plasma (known as jet ejecta), while the emission from the compact jet begins to switch off. With increasing accretion rates, the system is settled in the soft state, where most of the emission can be characterized by an optically thick, geometrically thin disk that extends down to the innermost stable circular orbit (Shakura & Sunyaev 1973), and locally emits a thermal blackbody spectrum. The compact jet emission in the soft state

is completely quenched (e.g., Russell et al. 2019c; Carotenuto et al. 2021). As the mass accretion rate decreases again, the system begins to transition back to the hard state, through the soft intermediate state (SIMS), where the compact radio jet emission is observed to recover.

The changing structure of inflows and outflows across accretion states manifests observationally as changes in the broadband (radio through X-rays) emission spectrum of BH XRBs. For this reason, multiwavelength observing campaigns play an important role in understanding the evolution of these sources throughout an outburst. During the rising phase of an outburst, when BH XRBs are found in the hard state, the jet component dominates the lower electromagnetic frequency broadband emission. This jet emission is characterized by a flat to slightly inverted optically thick spectrum ($f_\nu \propto \nu^\alpha$, where $\alpha \sim 0$), extending from radio to submillimeter frequencies and above (Corbel & Fender 2002; Casella et al. 2010; Tetarenko et al. 2015). The jet spectrum transitions from optically thick to optically thin emission (with $\alpha \sim -0.6$), which is observed as a spectral break at $\nu_b \sim 10^{11-14}$ Hz, (submillimeter/infrared frequencies; Russell et al. 2020). Thus, the compact jet component is typically modeled as a broken power law. Throughout this paper we refer to this spectral break, which results from synchrotron self-absorption, as the jet spectral break. There can also be a synchrotron cooling break at higher frequencies (e.g., Russell et al. 2014), resulting from the highest-energy electrons that radiate faster than the dynamical timescale of the system. At higher electromagnetic frequencies (optical to X-ray bands), the emission originates mainly from the accretion flow, and it is well described by an irradiated disk (Gierliński et al. 2008, 2009; Gilfanov 2010). In this model, the thermal disk provides seed photons that are intercepted by hot electrons in the inner flow (the corona). This interaction, known as inverse Compton scattering, results in a hard power-law spectrum with a high-energy cutoff in the range 20–100 keV, and photon indices $\Gamma \lesssim 2$. Some of these Comptonized photons can illuminate the disk, producing an iron emission line and Compton reflection component (e.g., Malzac et al. 2005).

As the source evolves into the intermediate states, the jet spectral break, initially located around the IR region, is observed to move toward lower electromagnetic frequencies (toward the radio wave bands; van der Horst et al. 2013; Russell et al. 2014, 2020b). The jet spectral evolution appears to be correlated with quenching of the compact jet

Table 1
Accretion States for all the Observed Epochs of J1820 during its 2018–2019 Outburst

Spectral State[a]	Color Code	Observed Epochs (2018)
Rising Hard	light/dark	March 16, 20
	blue	April 12, May 17
Intermediate	red/yellow	July 6, September 29
Soft	orange	July 13
Declining Hard	pink/purple	October 6, 11, 14, 19, 22, 26, 28
		November 3, 6, 10, 13, 18

Note.
[a] We use the accretion states defined in Shidatsu et al. (2019) for this work.

Table 2
Priors Used in the MCMC Simulations

Parameter	Model	Minimum Value	Maximum Value
Γ_1	bknpower	0.5	1.0
BreakE (keV)[a]	bknpower	0.	10^6
Γ_2	bknpower	1.5	1.8
BPL Norm	bknpower	0	10^{24}
kT_{disk} (keV)	diskir	0.01	5
L_c/L_d	diskir	0	10
f_{out}	diskir	0	0.1
Disk Norm	diskir	0	10^{24}
Γ[b]	diskir	...	...

Notes.
[a] For some epochs the priors on the energy break depend on the data available to constrain this parameter. See text for details.
[b] Priors for the X-ray photon index parameter, Γ, are taken from previous measurements in the literature. See Section 3.1 for details.

(Russell et al. 2020b). Discrete jet ejecta can also become detectable at this stage of an outburst (Corbel et al. 2004; Fender et al. 2004), but tend to display much brighter flux densities than the compact jet (e.g., Tetarenko et al. 2017). Some studies suggest that the breakup of the compact jet and the launching of ejections may be related to a change in the speed of the jet flow, leading to internal shocks when faster moving plasma catches up with slower moving plasma (Jamil et al. 2010; Malzac 2013, 2014). Alternatively, the ejecta may result from the ejection of the corona (Rodriguez et al. 2003; Vadawale et al. 2003; Rodriguez et al. 2008). In this scenario, the compact jet quenching might be related to the jet acceleration zone becoming disconnected from the system, and its propagation away from the source could explain the emergence of ejecta (Russell et al. 2020b). It has been suggested that these jet knots can be produced toward the end of the hard state in the rise of an outburst, during which time the corona may contract and become less vertically extended (e.g., Kara et al. 2019). Once in the HIMS (Fender et al. 2004, 2009), observations indicate that the coronal height increases, possibly representing material being ejected (e.g., Wang et al. 2022). In the simplest scenario, the corona extends above the disk, and is responsible for the hard X-ray emission, some of which is intercepted and reprocessed by the disk, producing a soft X-ray component. If the distance between the corona and the disk increases, the hard X-ray photons reach the observer before the soft ones, causing a delay known as soft reverberation lag. This delay is then a consequence of the changing disk–corona geometry and light travel times. Thanks to the high time resolution of the Neutron star Interior Composition ExploreR (NICER) X-ray Timing instrument, and its low energy coverage with a good effective area, such measurements have been possible (De Marco et al. 2021; Wang et al. 2021), providing the aforementioned insights into the corona–jet connection.

Once the source enters the softer states (SIMS and soft state), the broadband spectrum is dominated by the thermal disk, with a softer X-ray spectrum ($\Gamma \gtrsim 2$), and any radio emission detected is attributed to the remnants of the jet ejecta, or their collisions with the local interstellar medium (e.g., Corbel et al. 2002, 2004; Russell et al. 2019c; Bright et al. 2020; Carotenuto et al. 2021). As the outburst decays the source returns to the hard state (going through the SIMS and HIMS in reverse), but this time with lower luminosities (Maccarone 2003; Done et al. 2007). Over the soft-to-hard state transition at the end of the outburst, the compact jet is observed to reignite, first in the radio and then in the optical/IR bands (e.g., Miller-Jones et al. 2012;

Corbel et al. 2013; Kalemci et al. 2013; Russell et al. 2014, 2020), where the spectral break is observed to move in the opposite direction to the forward transition, i.e., from lower to higher frequencies (Russell et al. 2014).

The location of the jet spectral break and the flux density at that electromagnetic frequency are key pieces of information needed to understand the jet-launching mechanism and energetics (Heinz & Sunyaev 2003; Chaty et al. 2011; Polko et al. 2014; Ceccobello et al. 2018; Lucchini et al. 2021), since this break traces the jet base region where the particles are first accelerated (Markoff et al. 2001, 2005; Markoff 2010; Romero et al. 2017). For instance, accurate measurements of the spectral break can provide constraints on the cross-sectional radius and magnetic field strength at the base of the jet (Rybicki & Lightman 1979; Casella & Pe'er 2009; Chaty et al. 2011; Gandhi et al. 2011), although this is dependent on simple one-zone models. Tracking the spectral break location and its connection to changes in the accretion flow (probed through X-ray emission) require multiwavelength coverage of the broadband spectrum throughout different stages of an outburst. Observations exist for only a handful of systems so far: MAXI J1836–194 (Russell et al. 2013b, 2014), V404 Cygni (Tetarenko et al. 2019), and MAXI J1535–571 (Baglio et al. 2018b; Russell et al. 2020b). However, all of these previous works have only probed a portion of the jet evolution cycle during outburst. In this work, we present a multiwavelength data set during the 2018–2019 outburst of the BH XRB MAXI J1820+070, which has allowed us to track the broadband spectrum throughout a full outburst cycle, sampling the establishment, quenching, and reignition of the compact jet for the first time.

1.1. MAXI J1820+070

The Galactic BH XRB MAXI J1820+070 (ASASSN-18ey, hereafter J1820) was first detected in the optical band with the All-Sky Automated Survey for SuperNovae (Shappee et al. 2014; Kochanek et al. 2017), on 2018 March 6 (MJD 58184.079861; Tucker et al. 2018). Later, it was detected in X-rays with the Monitor of All-sky X-ray Image (MAXI; Matsuoka et al. 2009) Gas Slit Camera (Mihara et al. 2011) on 2018 March 11 (Kawamuro et al. 2018). The system was first identified as a likely BH XRB in outburst by Baglio et al. (2018c). The nature of the compact object was dynamically
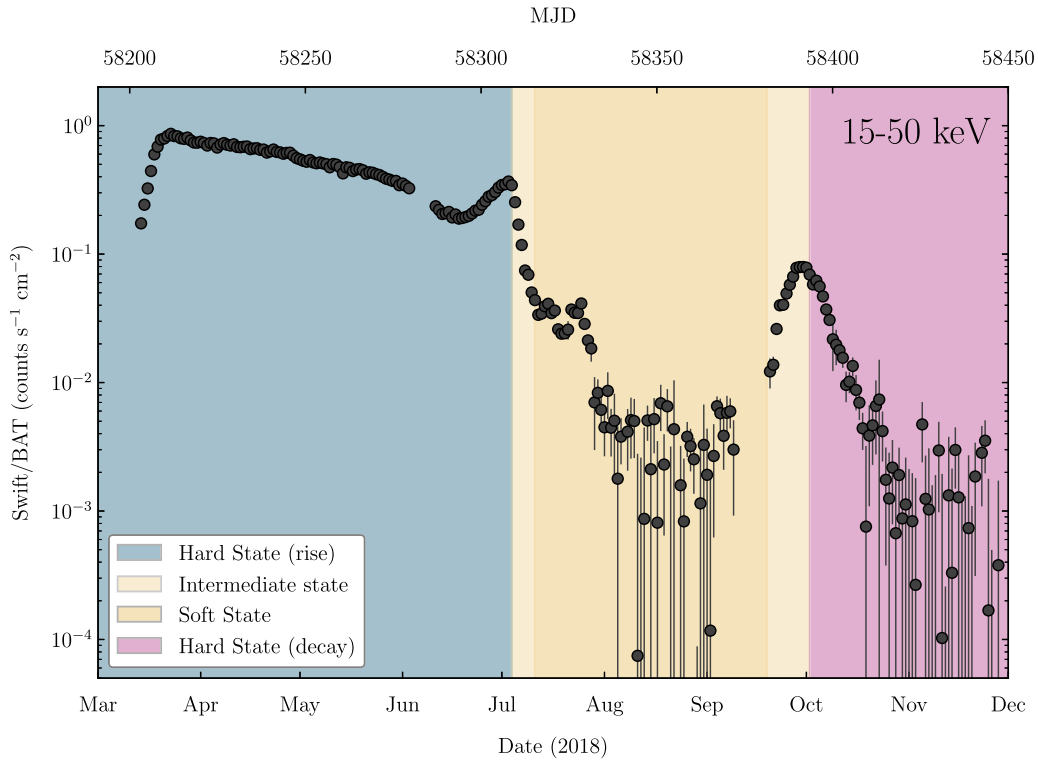
Figure 1. J1820 Swift/BAT daily light curve in the 15–50 keV energy range throughout its 2018–2019 outburst. Data were obtained from the BAT transient monitor (Krimm et al. 2013). The background shading represents the accretion states identified in Shidatsu et al. (2019): rising hard state (blue), intermediate and soft states (yellow), and declining hard state (pink).

confirmed by Torres et al. (2019), and later refined in Torres et al. (2020), to be a BH with $M_{BH} = 8.48^{+0.79}_{-0.72} \, M_{\odot}$. The system also hosts a type K3-5 companion with an orbital period of 16.5 hr. Thanks to its high X-ray flux $\sim 3.99 \times 10^{-8}$ erg cm^{-2} s^{-1} ($\sim$4 Crab in 20–50 keV; Roques & Jourdain 2019), its close distance (2.96 ± 0.33 kpc; Atri et al. 2020), and a low Galactic extinction ($N_H = 1.5 \times 10^{21}$ cm^{-2}; Uttley et al. 2018), the source was an excellent candidate for an extended multiwavelength campaign during its outburst.

J1820 remained in the hard state until a rapid softening of the X-ray spectrum on 2018 July 5 indicated it was entering the soft state (Homan et al. 2018b). During this state transition, the broadband emission was dominated by a thermal disk from optical to soft X-rays, while the radio to infrared flux decreased, suggesting quenching of the compact jet (Casella et al. 2018; Tetarenko et al. 2018). Additionally, strong radio flares were detected (Bright et al. 2018), consistent with the launching of jet ejecta (Bright et al. 2020; Wood et al. 2021). In late September, the X-ray spectrum exhibited spectral hardening (Homan et al. 2018a; Motta et al. 2018), suggesting that the source started its return to the hard state. In the following months the outburst continued to decay, reaching quiescence in 2019 February (Russell et al. 2019a). Since then, J1820 has shown little activity, with rebrightening episodes in 2019 (Bahramian et al. 2019; Bright et al. 2019; Hambsch et al. 2019; Ulowetz et al. 2019; Williams et al. 2019; Xu et al. 2019), 2020 (Adachi et al. 2020; Sasaki et al. 2020), 2021 (Baglio et al. 2021b), and a possible reactivation of the compact jet in 2022 (Carotenuto et al. 2022), but has not entered a full outburst again with state changes. The latest reports indicate that the source continues to fade into

quiescence (Baglio et al. 2023; Homan et al. 2023), and no other multiwavelength observations have since been reported.

Broadband spectral analyses have been performed of J1820's outburst in 2018. However, these analyses only sampled isolated epochs of the outburst, focusing mainly on the hard state (e.g., Rodi et al. 2021, on April 12), and/or a limited region of the electromagnetic spectrum (e.g., Shidatsu et al. 2018, 2019; Bharali et al. 2019; Chakraborty et al. 2020; Marino et al. 2021; Özbey Arabacı et al. 2022; Prabhakar et al. 2022; Cangemi et al. 2023). In this work, we characterize the broadband spectrum (from the radio to X-ray bands) of J1820 over the course of its full 2018 outburst, a period summarized in Figure 1. We place particular attention on the evolution of the spectral parameters of the jet, and their connection to the accretion flow parameters.

This paper is organized as follows. In Section 2 we describe the observations and reduction of each data set utilized in this work. The details of the spectral modeling are presented in Section 3, together with the best-fit broadband spectrum of each observational epoch. In Section 4 we discuss the evolution of the spectral parameters, focusing on those connecting the accretion flow to the jet. To date, this connection remains uncertain. We also compare J1820's evolution to the observed behavior of other BH XRBs in similar phases of their outbursts. Our analyses are complementary to the significant work that has been made in studying the time-domain properties of J1820 (e.g., Kara et al. 2019; Paice et al. 2019, 2021; Wang et al. 2020; Tetarenko et al. 2021; Zdziarski et al. 2021), some of which we discuss in Section 4.3. Finally, we summarize our conclusions and findings in Section 5.
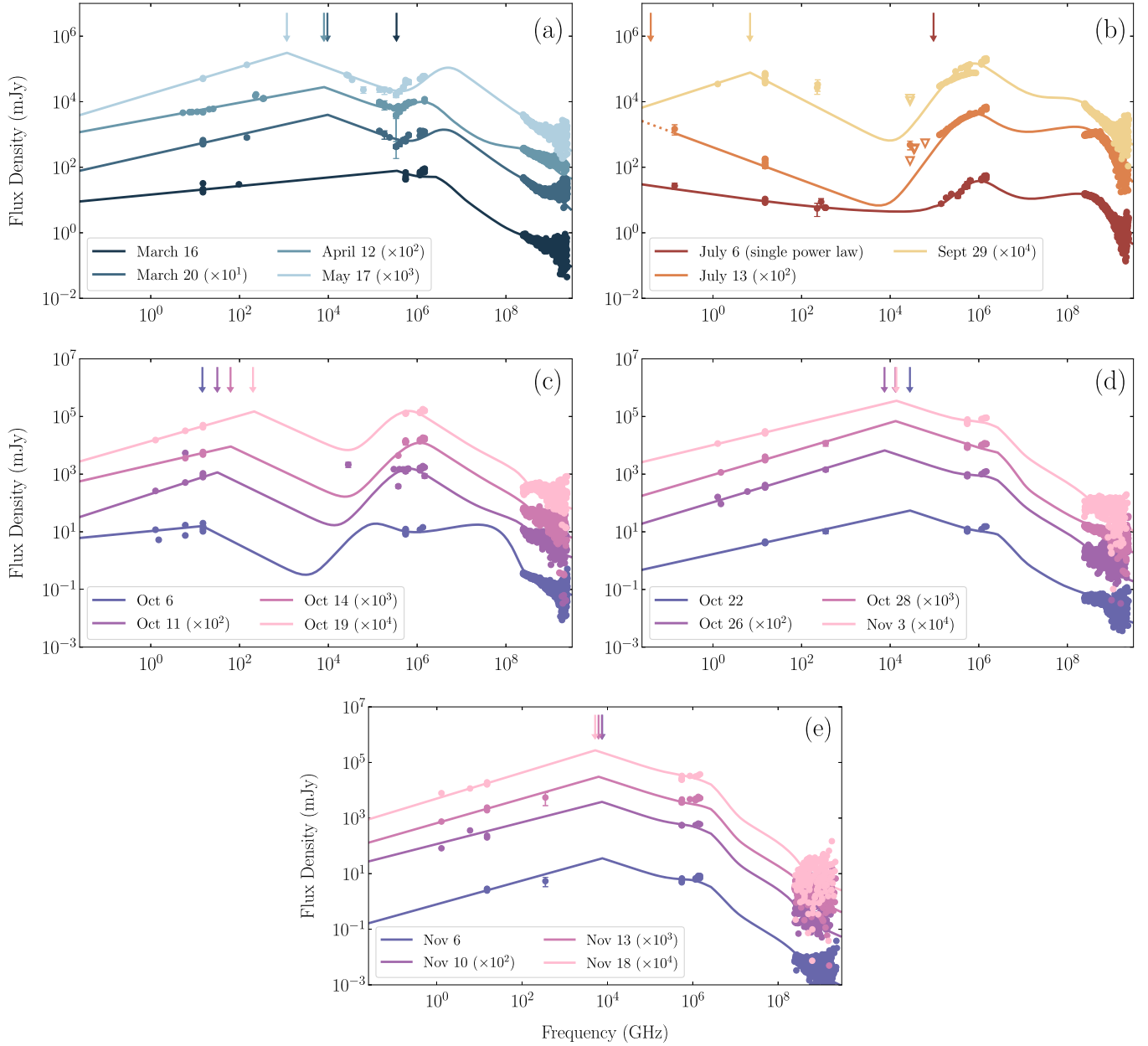
Figure 2. Broadband spectral evolution of J1820 over the course of its 2018–2019 outburst. In the panels of each spectrum, the points represent the data and the solid lines represent the best-fit model. We show the fit residuals in Figure 9. Colors indicate different epochs/accretion states and arrows mark the position of the spectral break for each individual epoch of the same color. The best-fit models and data points are scaled for better visualization, as identified in the legends (increasing with time). The optical, UV, and X-ray data are corrected for reddening and absorption. Panel (a) displays the broadband spectral models corresponding to the rising hard state (blue). Panel (b) shows the spectral models of the intermediate (July 6 and September 29) and soft (July 13) states (yellow). Panels (c), (d), and (e) show the spectral models corresponding to the declining hard state (pink). Note that the color codes for the accretion states are matched in Figures 1, 3, 4, and 6. The position of the spectral break on July 6 must be interpreted carefully since the jet contribution is modeled with a combination of emission from jet ejecta, which dominates at lower electromagnetic frequencies, and a fainter compact jet component (see Section 3.2.1). Similarly, on July 13, we do not have sufficient data at low frequencies to constrain the position of the spectral break. Thus, the arrow corresponds to an upper limit, and the dotted line is an extension of the power law above the break, reflecting our inability to predict its shape. On July 13 and September 29, the downward facing triangles represent upper limits on the VISIR data for these epochs, which are not included in the fit. We clearly observe different broadband spectral shapes of J1820 throughout the outburst.

2. Observations and Data Analysis

2.1. Radio, Submillimeter, and Millimeter

2.1.1. VLA

J1820 was observed with the National Radio Astronomy Observatory's (NRAO) Karl G. Jansky Very Large Array (VLA; project code: 18A–470) on 2018 April 12 (observing 6 hr on source). During these observations, the array was in the A configuration, and split into three subarrays, observing with the C (4–8 GHz), X (8–12 GHz), or K (18–26 GHz) bands. The correlator was set up in 8 bit mode and was comprised of two basebands, with eight spectral windows of 64 2 MHz channels each, giving a total bandwidth of 1.024 GHz per baseband. These VLA data were calibrated and imaged within the Common Astronomy Software Application package (CASA v5.4; McMullin et al. 2007). The flux densities of the source were measured by fitting a point source in the image plane

Table 3
Best-fit Parameters of the Multicomponent Phenomenological Model Obtained from Our MCMC Runs

Date (2018)	bknpower				diskir				
	α_{thick}	ν_b (Hz)	α_{thin}	BPL Norm ($\times 10^3$)	kT_{disk} (keV)	Γ	L_c/L_d	f_{out} ($\times 10^{-2}$)	Disk Norm ($\times 10^2$)
Mar 16	0.130 ± 0.002	$\leqslant 3.45 \times 10^{14}$	(-0.5)	$0.30^{+0.01}_{-0.01}$	0.79 ± 0.02	$\geqslant 1.49$	$9.97^{+0.02}_{-0.05}$	2.04 ± 0.09	$2.94^{+0.29}_{-0.27}$
Mar 20	$0.31^{+0.01}_{-0.02}$	$9.54^{+2.06}_{-1.11} \times 10^{12}$	(-0.5)	$14.98^{+4}_{-4.71}$	0.91 ± 0.01	$\geqslant 1.55$	$9.99^{+0.01}_{-0.03}$	$3.46^{+0.07}_{-0.06}$	$7.02^{+0.29}_{-0.27}$
Apr 12	0.2513 ± 0.0004	$7.98^{+0.06}_{-0.06} \times 10^{12}$	(-0.5)	6.16 ± 0.03	$0.423^{+0.006}_{-0.002}$	$\geqslant 1.6$	$9.98^{+0.02}_{-0.04}$	0.663 ± 0.006	$144.81^{+2.39}_{-2.38}$
May 17	0.408 ± 0.003	$1.16^{+0.03}_{-0.03} \times 10^{12}$	(-0.5)	$76.51^{+3.87}_{-3.75}$	$0.88^{+0.01}_{-0.01}$	$1.660^{+0.001}_{-0.001}$	$9.93^{+0.05}_{-0.10}$	6.45 ± 0.14	4.04 ± 0.12
Jul 6	0.12 ± 0.07	$\leqslant 1.53 \times 10^{14}$	(-0.7)	$\leqslant 0.03$	0.69 ± 0.01	$\geqslant 2.17$	0.66 ± 0.03	$0.193^{+0.004}_{-0.004}$	$164.72^{+6.25}_{-5.88}$
Jul 13	$0.45^{+0.04}_{-0.11}$	$\leqslant 1.40 \times 10^{8}$	(-0.5)	$\leqslant 6752$	0.542 ± 0.001	$\geqslant 2.60$	0.78 ± 0.01	0.244 ± 0.001	$361.38^{+1.94}_{-1.90}$
Sep 29	$0.44^{+0.04}_{-0.10}$	$6.88^{+1.60}_{-0.49} \times 10^{9}$	(-0.5)	$\leqslant 61$	0.297 ± 0.001	$1.94^{+0.03}_{-0.02}$	2.94 ± 0.11	$0.82^{+0.03}_{-0.02}$	$141.92^{+0.85}_{-0.83}$
Oct 6	0.152 ± 0.002	$\geqslant 1.46 \times 10^{10}$	$\geqslant -0.80$	$0.32^{+0.01}_{-0.01}$	0.101 ± 0.001	$\geqslant 1.68$	$0.98^{+0.05}_{-0.04}$	0.05 ± 0.01	$62810.96^{+3289.45}_{-3110.23}$
Oct 11	$\leqslant 0.50$	$\geqslant 2.06 \times 10^{10}$	$\geqslant -0.79$	$53.19^{+0.40}_{-0.77}$	0.153 ± 0.001	$\geqslant 1.63$	$9.95^{+0.04}_{-0.08}$	2.22 ± 0.03	$258.82^{+3.95}_{-3.98}$
Oct 14	0.355 ± 0.007	$\geqslant 2.80 \times 10^{10}$	$\geqslant -0.78$	$3.30^{+0.42}_{-0.37}$	0.199 ± 0.002	$\geqslant 1.62$	$9.96^{+0.02}_{-0.05}$	$6.19^{+0.16}_{-0.15}$	$40.05^{+1.45}_{-1.43}$
Oct 19	0.44 ± 0.01	$\geqslant 6.35 \times 10^{10}$	$\geqslant -0.77$	$12.24^{+2.81}_{-2.34}$	0.123 ± 0.002	$\geqslant 1.67$	$9.93^{+0.06}_{-0.11}$	$4.78^{+0.15}_{-0.14}$	$263.59^{+26.24}_{-23.30}$
Oct 22	0.34 ± 0.03	$2.79^{+0.86}_{-0.66} \times 10^{13}$	$\leqslant -0.51$	$\leqslant 3.4$	0.47 ± 0.02	$\geqslant 1.58$	$9.86^{+0.11}_{-0.22}$	$2.46^{+0.26}_{-0.24}$	$1.47^{+0.22}_{-0.20}$
Oct 26	0.464 ± 0.009	$7.46^{+0.91}_{-0.84} \times 10^{12}$	$\leqslant -0.5$	$13.82^{+2.17}_{-1.87}$	0.22 ± 0.02	$\geqslant 1.64$	$9.67^{+0.25}_{-0.50}$	$8.14^{+0.85}_{-0.79}$	$7.74^{+3.83}_{-2.41}$
Oct 28	0.45 ± 0.01	$1.32^{+0.12}_{-0.11} \times 10^{13}$	$\leqslant -0.5$	$9.92^{+2.12}_{-1.74}$	$0.60^{+0.03}_{-0.02}$	$\geqslant 1.66$	$9.72^{+0.21}_{-0.42}$	$4.32^{+0.27}_{-0.25}$	0.13 ± 0.02
Nov 3	$0.37^{+0.02}_{-0.01}$	$1.38^{+0.21}_{-0.19} \times 10^{13}$	$\leqslant -0.5$	$2.20^{+0.65}_{-0.47}$	0.19 ± 0.01	$\geqslant 1.75$	$9.72^{+0.21}_{-0.39}$	$\geqslant 9.47$	$7.58^{+3.42}_{-2.18}$
Nov 6	$0.42^{+0.04}_{-0.03}$	$7.52^{+1.80}_{-1.61} \times 10^{12}$	$\leqslant -0.5$	$5.01^{+4.36}_{-1.82}$	0.15 ± 0.01	1.78 ± 0.02	$9.71^{+0.21}_{-0.41}$	$\geqslant 9.71$	$14.27^{+4.91}_{-3.79}$
Nov 10	0.39 ± 0.01	$7.39^{+1.61}_{-1.59} \times 10^{12}$	$\leqslant -0.5$	$3.77^{+0.99}_{-0.75}$	$0.14^{+0.02}_{-0.01}$	$1.70^{+0.09}_{-0.06}$	$8.45^{+1.12}_{-1.83}$	$\geqslant 8.74$	$15.66^{+14.11}_{-8.09}$
Nov 13	0.44 ± 0.01	$6.17^{+0.70}_{-0.60} \times 10^{12}$	$\leqslant -0.5$	$5.41^{+1.40}_{-1.11}$	0.22 ± 0.01	$\leqslant 1.77$	$9.69^{+0.23}_{-0.48}$	$\geqslant 9.74$	$1.49^{+0.33}_{-0.28}$
Nov 18	0.47 ± 0.2	$5.13^{+0.83}_{-0.70} \times 10^{12}$	$\leqslant -0.5$	$7.05^{+2.34}_{-1.99}$	0.15 ± 0.01	$1.66^{+0.06}_{-0.04}$	$9.06^{+0.69}_{-1.33}$	$\geqslant 9.36$	$5.82^{+2.98}_{-2.34}$

Note. The jet component is modeled with bknpower, where α_{thick} represents the spectral index of the optically thick synchrotron emission, α_{thin} is the spectral index of the optically thin synchrotron emission, and BPL Norm is the normalization at 1 keV. The accretion flow is modeled with diskir, where kT_{disk} is the innermost temperature of the unilluminated disk, Γ is the photon index of the Comptonized X-ray emission, L_c/L_d is the ratio of the luminosity in the Comptonized emission (L_c) to the disk intrinsic luminosity (L_d), f_{out} is the fraction of flux intercepted by the outer disk, and Disk Norm is the disk normalization. The best-fit values are obtained from the median of the posterior distributions output from the MCMC runs, while the uncertainties are the 16% and 84% quantiles.

Table 4
Frequencies (ν_b) and Flux Densities (S_{ν_b}) at the Spectral Break, Obtained from Our Spectral Modeling (see Section 3.1)

Date (2018)	ν_b (Hz)	S_{ν_b} (mJy)
Mar 16	$\leqslant 3.45 \times 10^{14}$	$76.88^{+2.13}_{-2.09}$
Mar 20	$9.54^{+2.06}_{-1.11} \times 10^{12}$	$400.01^{+113.26}_{-110.24}$
Apr 12	$7.98^{+0.06}_{-0.06} \times 10^{12}$	$284.96^{+1.84}_{-1.80}$
May 17	$1.16^{+0.03}_{-0.03} \times 10^{12}$	$311.18^{+14.91}_{-14.27}$
Jul 6	$\leqslant 1.53 \times 10^{14}$	$194.58^{+394.14}_{-124.68}$
Jul 13	$\leqslant 1.40 \times 10^{8}$	$24.14^{+15.67}_{-9.48}$
Sep 29	$6.88^{+1.60}_{-0.49} \times 10^{9}$	$8.05^{+3.16}_{-3.64}$
Oct 6	$\geqslant 1.46 \times 10^{10}$	$16.08^{+0.23}_{-0.23}$
Oct 11	$\geqslant 2.06 \times 10^{10}$	$11.52^{+3.79}_{-2.23}$
Oct 14	$\geqslant 2.80 \times 10^{10}$	$9.26^{+3.71}_{-2.31}$
Oct 19	$\geqslant 6.35 \times 10^{10}$	$15.86^{+10.21}_{-6.06}$
Oct 22	$2.79^{+0.86}_{-0.66} \times 10^{13}$	$54.83^{+38.79}_{-21.17}$
Oct 26	$7.46^{+0.91}_{-0.84} \times 10^{12}$	$66.61^{+11.79}_{-9.91}$
Oct 28	$1.32^{+0.12}_{-0.11} \times 10^{13}$	$69.76^{+14.83}_{-11.94}$
Nov 3	$1.38^{+0.21}_{-0.19} \times 10^{13}$	$35.20^{+10.29}_{-7.36}$
Nov 6	$7.52^{+1.80}_{-1.61} \times 10^{12}$	$36.13^{+27.82}_{-12.76}$
Nov 10	$7.39^{+1.61}_{-1.59} \times 10^{12}$	$38.37^{+10.30}_{-8.35}$
Nov 13	$6.17^{+0.70}_{-0.60} \times 10^{12}$	$30.74^{+7.12}_{-5.70}$
Nov 18	$5.13^{+0.83}_{-0.70} \times 10^{12}$	$27.66^{+8.59}_{-7.13}$

(using the imfit task), and all flux density measurements are provided in Table 8. Further details on the observations and calibration of these data are provided in Tetarenko et al. (2021).

Refer to Section 2.1.7 for additional VLA data from the literature.

2.1.2. Atacama Large Millimeter/submillimeter Array

The Atacama Large Millimeter/submillimeter Array (ALMA) observed J1820 (project code: 2017.1.01103.T) between 2018 April 12 and July 6 (observing up to 5 hr on source per epoch). During our observations, the 12 m array was in its Cycle 5 C3 configuration, with 46 antennas, observing in Band 7 (central frequency of 343.5 GHz). The ALMA correlator was set up to yield 4×2 GHz wide basebands. These ALMA data were reduced and imaged within CASA. The flux densities of the source were measured by fitting a point source in the image plane (using the imfit task), and all flux density measurements are provided in Table 8. Details on the observations and calibration process of these data can be found in Tetarenko et al. (2021).

2.1.3. James Clerk Maxwell Telescope/SCUBA-2

The James Clerk Maxwell Telescope (JCMT; project code: M18BP025) observed J1820 between 2018 October 22 and November 14, in the 850 μm (350 GHz) and 450 μm (666 GHz) bands. The observations consisted of a series of ~30 minute scans on target with the SCUBA-2 detector (Chapin et al. 2013; Holland et al. 2013). To perform absolute flux calibration, observations of the calibrator CRL2688 were used to derive a flux conversion factor (Dempsey et al. 2013; Mairs et al. 2021). The daisy configuration was used to produce $3'$ maps of the target source region. During the observations,
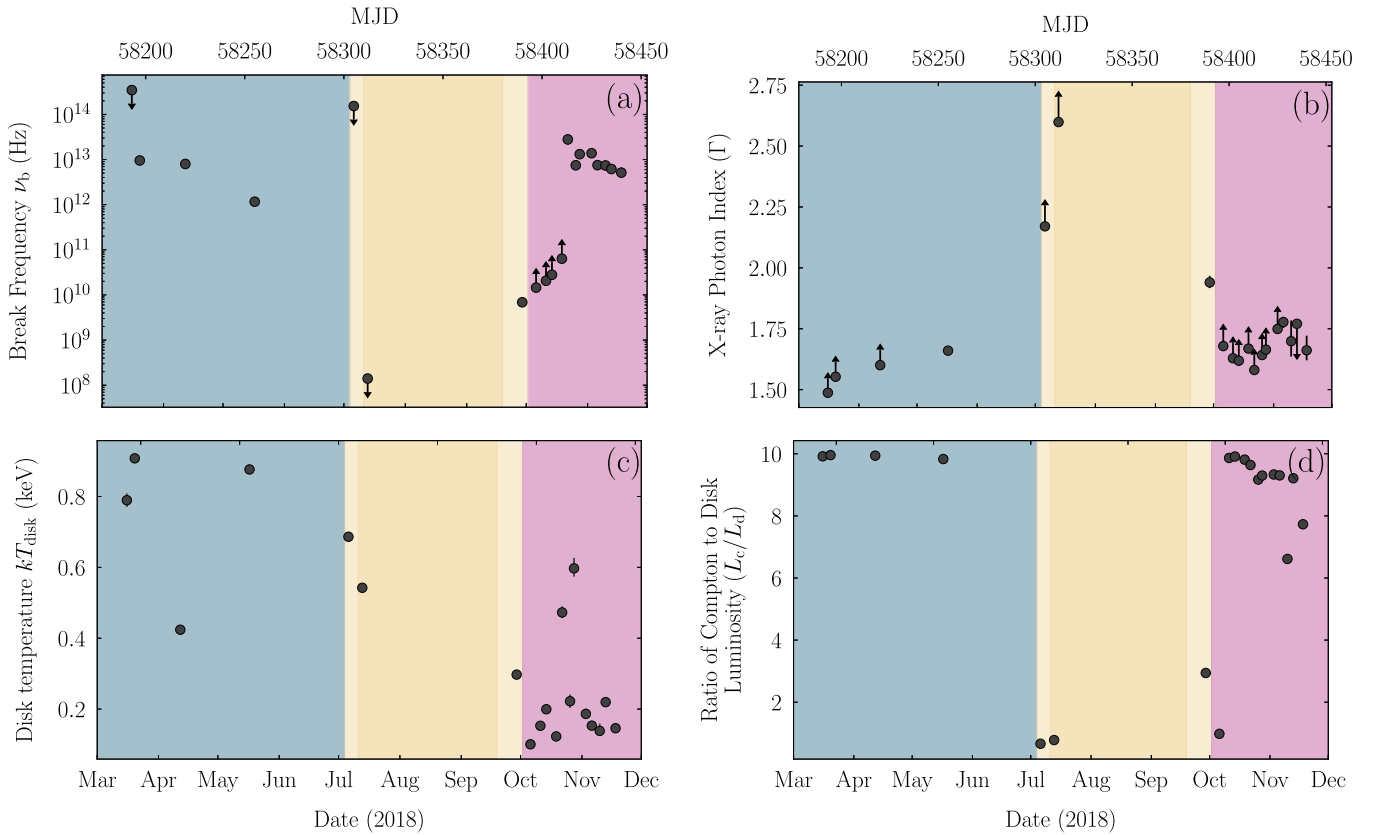
Figure 3. Evolution of the broadband spectral parameters of J1820 throughout its 2018–2019 outburst: the jet spectral break (ν_b, panel (a)), X-ray power-law photon index (Γ, panel (b)), disk temperature (kT_{disk}, panel (c)), and the ratio of the luminosity in the Comptonized emission to the disk intrinsic luminosity (L_c/L_d, panel (d)). Error bars are included for all data points, although in some cases these are smaller than the marker size. Arrows represent upper/lower limits. For L_c/L_d, we note that some values are consistent with the hard limit of the parameter ($L_c/L_d = 10$), but we omit the arrows for visualization. The background shading in all panels is matched to Figure 1, and represents the accretion states identified in Shidatsu et al. (2019): rising hard state (blue), intermediate and soft states (yellow), and declining hard state (pink). Note that the value of ν_b on July 6 must be interpreted carefully (see Section 3.2.1), as the spectrum is dominated by jet ejecta emission, preventing us from constraining the compact jet parameters accurately. All parameters show a distinct evolutionary pattern as the source progresses throughout the different accretion states of the outburst, and we observe an opposite trend in the evolution of the break frequency (ν_b) and the X-ray photon index (Γ).

the weather band was Grade 2 or 3 at the telescope, with a 225 GHz opacity of 0.05–0.12. Data were reduced with the STARLINK software package using both standard procedures outlined in the SCUBA-2 cookbook[45] and SCUBA-2 Quick-guide.[46] We note that the source was only detected at 850 μm, and all flux density measurements are provided in Table 8.

2.1.4. Institute de Radioastronomie Millimétrique's Northern Extended Millimetre Array

J1820 was observed with the Institute de Radioastronomie Millimétrique's (IRAM) NOrthern Extended Millimetre Array (NOEMA) under the project codes W17BN and W17BM in 2018. W17BN was observed first, and recorded data in three different bands: W17BN001 at 97.5 GHz was observed on 2018 March 16, W17BN002 at 140.0 GHz on 2018 March 20, and finally W17BN003 at 230.0 GHz also on 2018 March 20. At that time the interferometer was in extended configuration, and the observations were performed respectively with nine, eight, and eight antennas. Under W17BM the source was flux monitored at 140.0 GHz on 2018 May 10, May 18, and May 21 in compact eight, six, and eight antenna configurations, respectively. For amplitude and phase calibration we used the

quasars B1827+062 and B1749+096, and as flux calibrator the carbon star MWC349. The PolyFiX correlator was used in broadband mode, providing a bandpass of 7.744 GHz in dual linear polarization in both the upper and lower sidebands with 2 MHz resolution. The spectral bandpass was calibrated on different strong quasars, e.g., 3C279, 3C273, 3C84, B2013 +370, and B1749+096. Calibration of the NOEMA data was performed with the dedicated CLIC program that is part of the GILDAS[47] software package using standard procedures. All data were then exported to CASA[48] for imaging (using natural weighting to maximize sensitivity). The flux densities of the source were measured by fitting a point source in the image plane (using the `imfit` task). These measurements are presented in Table 8.

2.1.5. Sub-millimeter Array

The Sub-millimeter Array (SMA; project codes: 2017B-S010 and 2018A-S011) observed J1820 between 2018 April 12 and September 29 (observing up to 7 hr on source per epoch). All of our observations utilized the SWARM correlator in dual receiver mode, tuned to central frequencies of 224/230 GHz
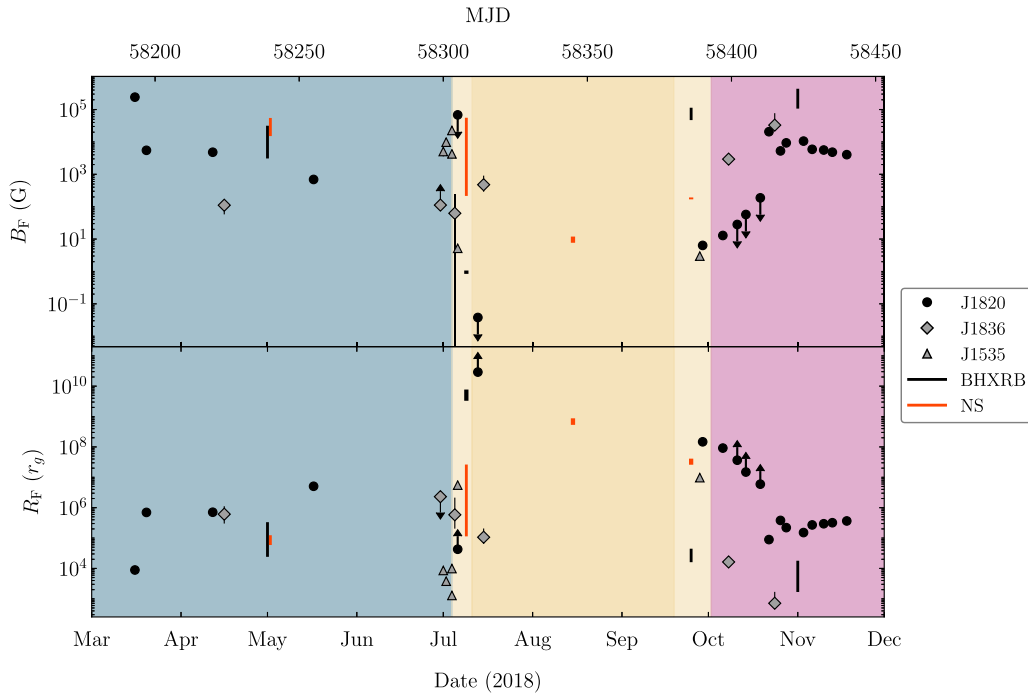

Figure 4. Evolution of the magnetic field (B_F, top panel) and distance (R_F, bottom panel) of the jet base (where particle acceleration begins) of the J1820 compact jet during the 2018–2019 outburst. R_F is measured in units of gravitational radii, where $M_{BH} = 8.48\,M_\odot$ was used (Torres et al. 2020). Measurements for J1836 (Russell et al. 2014) and J1535 (Russell et al. 2020b) are included as gray diamonds and triangles, respectively. We include ranges of B_F and R_F values for other BH XRBs and NSs with spectral break measurements, and represent them with black and red bars, respectively. For visualization purposes, we arbitrarily scaled the epochs of all sources to match similar phases of J1820's outburst. The background shading represents the accretion states as described in Figure 3. The overall behavior is consistent with that observed for J1836, J1535, NSs, and other BH XRBs in similar phases of their outbursts, where the compact jet is quenched toward the state transition and recovered during the outburst decay.

for RxA/RxB, with seven or eight antennas observing in the array. This setup yields two 8 GHz sidebands per receiver, giving a total bandwidth of 32 GHz. The SMA data were converted to CASA measurement set format using custom scripts provided by SMA.[49] Then all flagging, calibration, and imaging (using natural weighting to maximize sensitivity) of the data were performed within CASA using procedures outlined in the CASA Guides for SMA data reduction.[50] We used 3C454.3, 3C279, and 3C345 as bandpass calibrators, J1743+038 and J1751+096 as phase calibrators, and Neptune, Titan, and Callisto as flux calibrators.[51] The flux densities of the source were measured by fitting a point source in the image plane (using the `imfit` task), and all flux density measurements are provided in Table 8.

2.1.6. Arcminute Microkelvin Imager Large Array

J1820 was also observed with the Arcminute Microkelvin Imager Large Array (AMI-LA; Zwart et al. 2008; Hickish et al. 2018) during the 2018–2019 outburst. Observations were carried out at a central frequency of 15.5 GHz with 4096 channels spanning the range 13–18 GHz. The raw data from the correlator were binned into 8 × 0.626 GHz channels to produce "quick-look" data which were reduced by the custom software REDUCE_DC, which includes flagging of hardware errors and radio frequency interference and performs flux, bandpass, and complex gain calibrations (using 3C286 and J1824+1044).

Additional flagging and imaging were performed using CASA. The flux density of J1820 was measured using the CASA task IMFIT. Here we use a subset of the AMI-LA observations taken during this outburst, which were quasi simultaneous with our other multiwavelength measurements. We note that the AMI-LA resolution is not sufficient to be able to resolve discrete jet ejections or distinguish the core compact jet from the ejections. Therefore, the AMI-LA flux density may be a combination of the compact jet and the jet ejections. While this is not an issue for the hard state observations, it may impact transition and soft state observations. All flux density measurements can be found in Table 8.

2.1.7. Additional Data from the Literature

We include additional long-wavelength data found in the literature from the Low Frequency ARray (Broderick et al. 2018), the Karoo Array Telescope (Bright et al. 2020), the Multi-Element Radio Linked Interferometer Network (eMER-LIN; Bright et al. 2020), the VLA (project code: 18A–277; Shaw et al. 2021), and the Very Long Baseline Array (VLBA, project code: BM467; Atri et al. 2020) facilities. The details of all these data sets are presented in Table 8.

2.2. Infrared/Optical/UV

2.2.1. Very Large Telescope/VISIR

Mid-infrared observations of the field of J1820 were made with the Very Large Telescope (VLT) on 14 dates from 2018 April to October, under the programs 0101.D-0634 and 0102. D-0514 (PI: D. Russell). The VLT Imager and Spectrometer for the mid-InfraRed (VISIR; Lagage et al. 2004) instrument on
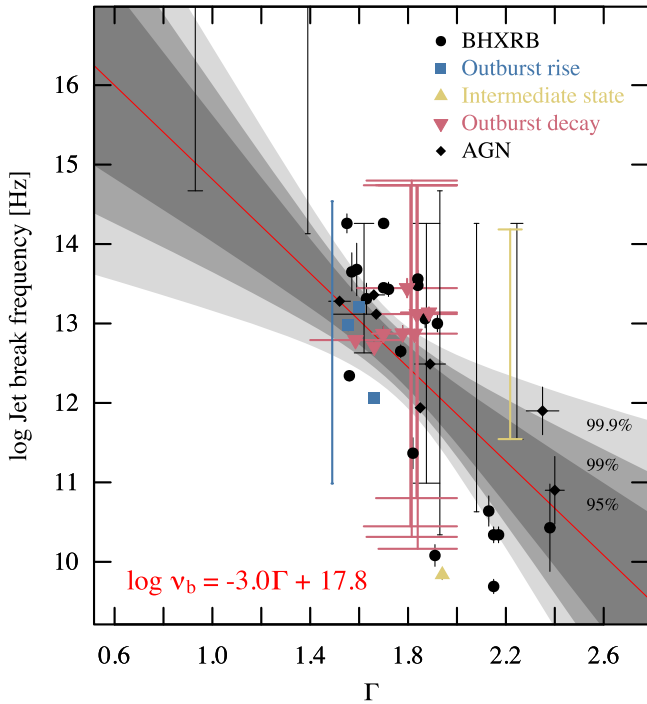

Figure 5. Measurements of the relationship between the jet spectral break frequency (ν_b) and the X-ray power-law photon index (Γ). Black circles represent measurements of other BH XRB sources from the literature, while black triangles correspond to AGN measurements from the literature (see Koljonen et al. 2015; Torres et al. 2020). J1820's measurements presented in this work are shown as blue (rising hard state) and pink (declining hard state) squares, where bars indicate data with only limits on ν_b (vertical) and Γ (horizontal). The dark shaded regions represent the 95%, 99%, and 99.9% confidence intervals of a linear regression fit to all of the data, including J1820 (Koljonen et al. 2015). Our measurements of J1820 are in good agreement with the relationship observed for other sources (with the exception of epochs with weak constraints on the jet spectral break), suggesting a similar mechanism governs the accretion flow and jet changes (see Section 4.3).

Figure 6. Evolution of soft X-ray lags (orange squares, top panel) and soft X-ray lags of quasi-periodic oscillation (QPO) frequencies from Stiele & Kong (2020; orange circles, bottom panel) compared to the evolution of the jet spectral break (dark gray markers). The background shadings correspond to the accretion states described in Figure 3. The evolutions of the QPO frequency and soft X-ray lags appear to be inversely correlated with the jet spectral break evolution, and thus is suggestive of a connection between the accretion inflow and jet outflow.

the VLT was used in small-field imaging mode (the pixel scale was 45 mas pixel^{-1}). Five filters (M, J8.9, B10.7, B11.7, and Q1) were used on different dates, with central wavelengths of 4.67, 8.70, 10.64, 11.51, and 17.65 μm, respectively (see also Russell et al. 2018). For each observation, the integration time on source was composed of a number of nodding cycles, with chopping and nodding between the source and sky. The total observing time was typically almost twice the integration time.

Observations of standard stars were made on the same nights as the target, in the same filters. All data (target and standard stars) were reduced using the VISIR pipeline in the *gasgano* environment. Raw images from the chop–nod cycle were recombined. Photometry was performed on the combined images using the `phot` task in IRAF, with an aperture large enough that small seeing variations did not affect the fraction of flux in the aperture. For some standard star observations, ESO provided pipeline-reduced images and counts/flux ratio values. Our counts/flux ratio values calculated separately agree with those of ESO's pipeline to a level of 0.4%–2.4%, for those standards, in all filters, with no apparent change with differing seeing. The standards were used to estimate the counts/flux ratio needed to convert the count rates to flux densities. Some standard star observations were rejected due to a nearby star overlapping with the point-spread function (PSF) of the standard (this was the case for standards HD 075691 and HD 000787), or because they were observed during twilight.
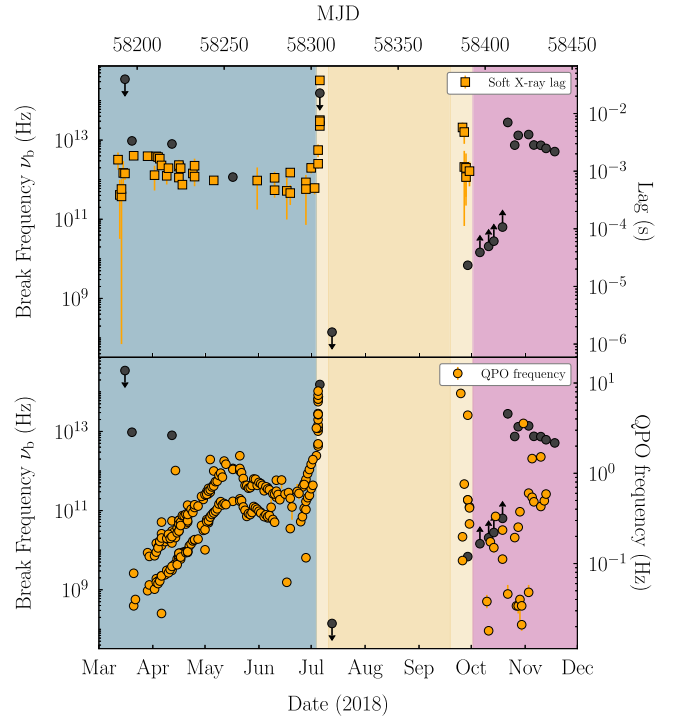
Since we have so many standard star observations, we investigate the variations in the counts/flux ratio throughout the whole observing period. The overall long-term and night-to-night stability of the photometric calibration of VISIR is known to be good (Dobrzycka et al. 2012). From the tests we carried out, under photometric conditions the sky transparency variations are less than a few percent (similar results were found in Baglio et al. 2018b). However, under poorer conditions, airmass and visibility affect some of our observations. For our observations taken in 2018, we find that the counts/flux ratio for the standards changed by >10% (and sometimes by much larger amounts) if either (a) the conditions were poor (thin or thick cloud, or high winds) or (b) the airmass was greater than 1.4. For the remaining observations (clear conditions, no strong wind, airmass $\leqslant$ 1.4), we find that the counts/flux ratio agreed on all dates, for all standards, to a level of $\pm6\%$, $\pm4\%$, $\pm4\%$, $\pm3\%$, and $\pm2\%$ compared to the mean value for the M, J8.9, B10.7, B11.7, and Q1 filters, respectively. These low-level variations in the conversion factor in the standards from night to night are likely due to intrinsic differences between the conversion factors derived for different standard stars, or possible background variations due to the water vapor content of the atmosphere above Paranal. There also appears to be no trend between the counts/flux ratio and time, or with airmass for airmass values $\leqslant$1.4. For standards taken at higher airmass (1.4–1.9) under clear conditions, we find that the counts/flux ratio differed by up to 8% from the mean value.

For the target observations, to convert counts to flux densities in millijanskies, we adopt the mean value of the

counts/flux ratio for each filter (for all standards taken under good conditions as explained above), for all target observations taken in clear conditions with airmass ⩽ 1.4. The error on the flux incorporates the error on the photometry (due to the signal-to-noise ratio of the target) and the standard deviation of the counts/flux ratio (a systematic error) combined in quadrature. For observations of the target taken in poor conditions (thin or thick cloud, high wind, or airmass > 1.4) we individually evaluate these carefully. In particular, the data on 2018 April 21 were observed under thick cloud and airmasses of 1.70–1.77. Nevertheless, enough standards were observed before and after the target, in each filter, that we are able to assess the variations of the counts/flux ratio due to clouds, and assess that the ratio of the airmass of the target and standards could cause a factor of 1.69 ± 0.69 uncertainty in cloud cover for the M band and similar uncertainties for the $J8.9$, $B10.7$, and $B11.7$ filters. We incorporate these uncertainties into the error calculations for the data taken on this date. Additionally, on 2018 May 11 high winds affected the counts/flux ratio; for this date we calibrate the target observations using the standards taken on the same date only, using the variations of the counts/flux ratio before and after the target observations to estimate the error contribution. The results are shown in Table 9.

2.2.2. Very Large Telescope/X-shooter

We undertook an observing campaign of the 2018 outburst of J1820 using the X-Shooter instrument at ESO's VLT (project code: 0101.D-0356; Vernet et al. 2011). The nine observing epochs spanned different accretion states throughout the outburst (hard, soft, and intermediate). Depending on the source intensity, each observation consisted of either five, four, or two exposures arranged in AB pairs alternating between the source and sky positions with a nod throw length of 5″ and a jitter box of 1″. The exposure time for each observation was ∼45 minutes in aggregate. We use the i'-band filter for the slit acquisition and correcting the normalization of the X-Shooter spectra due to slit losses. We use slit widths of 1″.3, 1″.3, and 1″.2 for the UV, VIS, and NIR arms, respectively, and the detector readout mode was selected to be 100k/1pt/hg/1x2. We reduce the X-Shooter data with ESO pipeline v3.5.0 in ESOREFLEX (Freudling et al. 2013). Telluric absorption is corrected using MOLECFIT (Kausch et al. 2015; Smette et al. 2015). Since this work focuses only on the continuum emission, and due to the high spectral resolution of X-Shooter, we bin the data to a few tens of data points, where the representative values correspond to the mean and standard deviation in each bin. The resulting data sets are presented in Table 10.

2.2.3. Las Cumbres Observatory and Al Sadeem Observatory

We monitored J1820 during its 2018 outburst extensively with the Las Cumbres Observatory (LCO) optical network of robotic telescopes (e.g., Baglio et al. 2018a, 2018c; Russell et al. 2018, 2019b). This is part of an ongoing monitoring campaign of ∼50 low-mass XRBs coordinated by the Faulkes Telescope Project (Lewis et al. 2008; Lewis 2018). The monitoring of J1820 includes data taken at the 1 m LCO telescopes at Siding Spring Observatory (Australia), Cerro Tololo Inter-American Observatory (Chile), McDonald Observatory (Texas), and the South African Astronomical Observatory (South Africa), as well as the 2 m Faulkes Telescopes at

Haleakala Observatory (Maui, Hawai'i, USA) and Siding Spring Observatory (Australia). Images were taken in the Sloan Digital Sky Survey (SDSS) g', r', and i' and Pan-STARRS Y-band filters (spanning 477–1004 nm central wavelengths). Here, data are included that were acquired within ∼1 day of the VISIR observations.

The data are initially processed using the LCO Banzai pipeline (McCully et al. 2018). Photometry is performed on the reduced data using the real-time data analysis pipeline XB-NEWS (see Russell et al. 2019b; Goodwin et al. 2020; Pirbhoy et al. 2020). The XB-NEWS pipeline downloads new images of targets of interest from the LCO archive along with their associated calibration data, performs several quality control steps to ensure that only good quality images are analyzed, and computes an astrometric solution for each image using Gaia DR2 positions.[52] Aperture photometry is then performed on all the stars in each image, solving for zero-point calibrations between epochs (Bramich & Freudling 2012), and flux calibrating the photometry using the ATLAS All-Sky Stellar Reference Catalog (Tonry et al. 2018). The pipeline also performs multiaperture photometry (azimuthally averaged PSF profile fitting photometry; Stetson 1990) for point sources. We detect the source with high significance throughout the outburst; during the epochs of interest the magnitude varied from $g' = 12.1$ and $i' = 12.4$ to $g' = 14.6$ and $i' = 14.2$.

We also monitored the source extensively with the Al Sadeem Observatory[53] (see also Baglio et al. 2018a; Russell et al. 2018, 2019b; Baglio et al. 2019, 2021a). The observatory is located in Al Wathba South, outside the city of Abu Dhabi in the United Arab Emirates. A Meade LX850 16 inch (41 cm) telescope was used, using an SBIG STT-8300 camera with Baader LRGB CCD filters (blue, green, and red filters with similar central wavelengths as the g', V, and R bands). Bias and flat-field images were combined, and the science images were reduced using these images. Photometry is then performed on the science images, using the PHOT task in IRAF. Several stars from the APASS catalog (Henden et al. 2012) in the field were used for flux calibration. For R band, we derive the R magnitudes of the field stars from the APASS g', r', and V magnitudes, adopting the conversions of Jordi et al. (2006).

2.2.4. Rapid Eye Mount

The Rapid Eye Mount (REM; Covino et al. 2004) is a 60 cm robotic telescope, located at the ESO-La Silla Observatory, and is equipped with an optical camera (ROS2; Molinari et al. 2014), and an IR camera (REMIR; Vitali et al. 2003). The two cameras observe simultaneously in the same field of view (∼10′ × 10′) thanks to a dichroic placed before the telescope's focal plane.

ROS2 observed J1820 simultaneously in its four filters (Sloan/SDSS g', r', i', and z'), and with REMIR we cycled through the J, H, and K filters (project code: 37025); see Table 9 for all REM measurements. All the observations, as well as the preliminary reduction and calibration procedures are carried out in a fully automated way by the robotic system with the Automatic QUick Analysis (AQUA; Testa et al. 2004) pipeline. The resulting products are preprocessed images and initial catalogs. Both the ROS2 and REMIR frames are astrometrically calibrated.

---

[52] https://www.cosmos.esa.int/web/gaia/dr2
[53] http://alsadeemastronomy.ae/

REMIR acquires a series of 30 s long frames by rotating a filter wedge along the optical path, thus obtaining five displaced images which are then combined together by median filtering. The resulting "empty sky" image is subtracted from each original frame. The five (sky subtracted and flat fielded) frames are then registered and summed, obtaining the final science image. Through this process, a final exposure of 150 s is reached for each of the filters. These resulting final images were reduced and analyzed with the PSF–fitting photometry package DAOPHOT (Stetson 1987), and calibrated against the Two Micron All Sky Survey catalog.

ROS2 has a multichannel system that splits the light in four different beams feeding four quadrants of a $2k \times 2k$ CCD equipped with four filters: g', r', i', and z'. The four images are thus acquired simultaneously, with an exposure of 180 s, and then reduced and calibrated using standard procedures with bias and flat-field frames obtained at twilight or during the daytime. The field of- view of ROS2 is approximately 9.1×9.1 arcmin^2 with a pixel scale of $0\farcs58$ pixel^{-1}. The ROS2 calibration was performed via secondary standards in the field on objects having SDSS or Pan-STARRS magnitudes. Photometric standards are also taken on every candidate photometric night, and a calibration relation is derived with zero-points, color term, and atmospheric extinction term. This service is provided by the observatory as another data product.

2.2.5. American Association of Variable Star Observers

We include additional optical data from the American Association of Variable Star Observers (AAVSO) international database (Kafka 2021), in the the the B (0.44 μm), V (0.55 μm), and I (0.80 μm) bands. Here we collect the photometry available within 1–2 days before and after the main date of our broadband spectra. For the dates with several entries, we average the measurements to get a single magnitude representative of each date with errors corresponding to the standard deviation. The average value is then converted into a flux density. A summary of the results can be found in Table 9.

2.2.6. Swift/UVOT

The Ultra-violet Optical Telescope (UVOT) instrument on board The Neil Gehrels Swift Observatory (Swift) observed J1820 simultaneously with the X-ray Telescope (XRT) throughout a good portion of its 2018 outburst. The exposures span across 7 months, and in most cases include data from the six filters available from the UV (UW1, UM2, and UW2) and optical (V, B, and U). To analyze UVOT observations we use the HEASOFT software v6.25[54] and followed the guidelines provided in the UVOT Data Analysis Guide.[55]

We first run the task uvotdetect on the images to obtain the centroid position of the source. To match the UVOT calibration, we select circular regions of $5''$ centered on the uvotdetect position to define the source extraction region. For the background we use a circular aperture of $20''$, chosen near the source and ensuring that the regions are not contaminated by nearby sources. Aperture photometry is performed using the task uvotsource to extract counts from those regions. Due to the counting nature of the CCD detectors, the UVOT instrument suffers from coincidence loss

(Fordham et al. 2000), a similar phenomenon to X-ray pileup. Coincidence loss occurs when multiple photons arrive at the same pixel within one readout frame of the detector. Since only one photon is recorded instead of two (or more), the true photon flux is underestimated. Furthermore, in the case of bright sources, the UVOT PSF is highly distorted. Because this effect is more likely to occur at high rates, we first analyze the count rate of the source and background regions in all our exposures. Following the analysis of Breeveld et al. (2010), we discard all observations with source count rate higher than $\sim$40 counts s^{-1}, and background count rate higher than 0.01 counts s^{-1}. The observations that are simultaneous to XRT (see below) are detailed in Table 5, while the nonsimultaneous observations are summarized in Table 6. Once we have the final exposures corrected for this effect, we obtain flux densities for all of them. These are summarized in Table 11. The reported fluxes include 1σ statistical errors, and the systematic uncertainty that arises from the shape of the instrument's PSF. As a result, we have a total of 40 UVOT observations simultaneous with XRT observations, totaling 130 flux density measurements.

2.3. X-Rays

2.3.1. Swift/XRT

The 20 X-ray exposures simultaneous with the UV are presented in Table 7, all of which were taken in the Window Timing (WT) mode. We first run the HEASOFT task xrtpipeline to build the standard data products with the latest calibration applied. On each event file, we select a circular region with a 30 pixel radius for both the source and background regions. Using xselect we extract count rates and build the source and background spectra, filtering grade 0 events to reduce the effect of pileup. However, in WT mode pileup becomes important for intensities $\sim$100 counts s^{-1} and above. Therefore, given the count rate of some of the observations, further pileup analysis is required.

To determine the level of pileup we follow the Swift/XRT analysis threads[56] for WT mode, specifically the spectral distortion method (also described in Romano et al. 2006). The analyses are performed using the X-ray Spectral Fitting Package (XSPEC v12.10.1; Arnaud 1996).

The overall effect of pileup is distortion in the shape of the spectrum, because multiple soft energy photons are stored as a single high-energy photon. As a result, we find an excess of high-energy photons as the power-law X-ray spectrum hardens, i.e., the photon index decreases. To mitigate this problem we select an annular source region, in which the inner circle corresponds to an exclusion region. This means that counts within the inner circle are not considered in the count extraction. The size of the inner circle can be varied to increase or decrease the count rate within the extraction region. Thus, each size defines a new source region from which a spectrum will be extracted. By fitting a power law to the X-ray spectrum, it is possible to study the behavior of the photon index (slope) parameter as the extraction region changes, which allows us to determine the level of pileup. When increasing the size of the inner circular region no longer impacts the value of the photon index, the region affected by pileup has effectively been excluded. Once the final pileup-corrected source region is

---

determined, we modify the size of the background regions to match the size of the new source region (as this is required for WT data), and reextract the source and background X-ray spectra. We then build the ancillary response files through the `xrtmkarf` task, which shows the corresponding redistribution matrix file as well. We finalize the process using `grppha` of FTOOLS[57] (Blackburn 1995) to assign bad channels (0–29) and group the spectra to a minimum of 20 counts bin^{-1}. This number of counts allows us to use χ^2 statistics by ensuring Gaussian errors in each bin. In addition to the bad channels, we decided to ignore all channels below 1.0 keV due to uncertainties in the low-energy regime of the WT data[58] to prevent any further effects of pileup, as well as channels above 10 keV.

2.4. Broadband Spectra

To construct our broadband spectra, each epoch is defined on the basis of the radio/submillimeter observations, where we collect optical to IR, UV, and X-ray data within ± 2 days of these data. In this way, the data are grouped in 19 representative epochs of the outburst. The accretion states of J1820 during its 2018 outburst are characterized by Shidatsu et al. (2019), using observations from MAXI/GSC and Swift/Burst Alert Telescope (BAT), and are shown in Table 1.

3. Results

In this section, we outline the phenomenological model applied to describe the 19 broadband spectra of J1820, as well as the fitting methodology and the results of our broadband spectral modeling.

3.1. Spectral Modeling

We use XSPEC to model the broadband spectrum across multiple epochs. To model each epoch (containing data from radio to X-rays) in the same model phase space in XSPEC, we first create spectrum files for all the data. The spectrum files corresponding to radio/submillimeter, IR, and optical data are created using the tool `flx2xsp` available through FTOOLS. For the UV data, the UVOT software employs its own routine `uvot2pha`, which allows us to create spectral files from UVOT images. For the X-ray data, we directly use the instrument response and spectrum files obtained from the procedure described in Section 2.3.

The multicomponent phenomenological model (see Figure 8) we employ to describe the broadband spectra consists of (1) a broken power law (`bknpower`[59] in XSPEC), representing synchrotron emission from the compact jet in the radio to IR bands, with a high-energy cutoff (`highecut` in XSPEC) to prevent the synchrotron emission from extending unbroken into the X-ray bands, since the cooling break is expected to lie somewhere below X-rays; (2) a blackbody (`bbodyrad` in XSPEC), representing emission from the stellar companion in the optical band; ad (3) an irradiated disk (`diskir` in XSPEC), representing accretion flow emission in the optical to X-ray bands (which combines the `diskbb` and `thcomp` models; Gierliński et al. 2008, 2009). Additionally,

absorption due to the presence of gas and dust in the interstellar medium is modeled with `redden` acting on the IR/optical/UV bands (Cardelli et al. 1989), and `tbabs` (Wilms et al. 2000) acting on the X-ray bands. The full phenomenological model in XSPEC formalism is `redden * tbabs (highecut * bknpower + bbodyrad + diskir)`.

In our model, we have 19 total parameters,[60] where up to 11 of these parameters are fixed to known or expected values. In particular, the absorption parameters $E(B - V) = 0.18$ (Tucker et al. 2018) and $N_H = 1.5 \times 10^{21}$ cm^{-2} (Uttley et al. 2018) are fixed to their known values in the direction of the source. The `highecut` energy and e-folding energy were both fixed at 0.01 keV. The `bbodyrad` model parameters (surface temperature and normalization) are also fixed based on the known companion star spectral type (K3-5; Torres et al. 2019) and the known distance to J1820 (Atri et al. 2020). The parameters from the irradiated disk portion of the model that are fixed across all epochs to typical BH XRB values from the literature (e.g., Gierliński et al. 2008) include the temperature of the corona $T_e = 100$ keV, the radius of the illuminated disk $R_{irr}/R_{in} = 1.2$ (where R_{in} is the disk inner radius), the fraction of luminosity in the Compton tail that is thermalized in the inner disk $f_{in} = 0.1$, and the radius of the outer disk $\log(R_{out}/R_{in}) = 4.5$. Lastly, in some epochs we need to fix the spectral index of the optically thin piece of the `bknpower` jet emission model to standard values ($\alpha_{thin} = -0.5$), as we do not have enough data to constrain this parameter accurately.

The broadband spectra are fit individually with the XSPEC implementation of a Markov Chain Monte Carlo (MCMC) algorithm (where XSPEC uses the Goodman–Weare algorithm; Goodman & Weare 2010). To initialize the parameters for each MCMC run, we manually explore the parameter space for our best-sampled epoch (April 12) to determine a reasonable initial guess for the MCMC algorithm. For each MCMC run, we standarized the number of walkers to 14 per free parameter and run the chains for 10^6 steps, with a burn-in corresponding to 30% of the chain length, since this was sufficient for the chains to converge. The convergence of the parameters is assessed with the Geweke convergence criteria (Geweke 1992) that is output by `chain` in XSPEC, as well as visually inspecting the chains of each parameter and the posterior distributions (see, for example, Figure 7). The best-fit parameters reported correspond to the median of the posterior distribution and the uncertainties represent the 68% confidence interval, i.e., the 16% and 84% quantiles of the posterior distribution.

The priors used for each model parameter are outlined in Table 2. The majority of our chosen priors are based on typical values observed for BH XRBs. For example, to describe the shape of the broken power-law jet emission spectrum, typical photon index ranges are $\Gamma_1 = 0.5$–1, and $\Gamma_2 = 1.5$–1.8, and thus the resulting priors used are uniform distributions covering these ranges. However, for the photon index of the X-ray spectrum (Γ), we use measurements reported in previous works of J1820 in the literature: You et al. (2021) for the rising hard state, Shidatsu et al. (2019) for the intermediate/soft states, and Shaw et al. (2021) for the declining hard state, where the priors are also uniform. In some of our epochs the jet spectral break

---

priors are adjusted according to the available data. For instance, on July 13 the spectral break cannot be higher than ~0.14 GHz (our first radio data point). Similarly, for October 6–19, the sparse data in the radio–IR region prevents us from accurately constraining the jet spectral break. Thus, we use as priors the last radio data point at ~15 and ~10^5 GHz (start of optical band). The best-fit models are shown in Figure 2 and the best-fit parameters are listed in Table 3 (refer to Table 4 for the flux densities at the spectral breaks).

3.2. Analysis of Spectra in Transition States

Among the broadband spectra analyzed in this work, special care is taken during the transition (July 6) and soft state (July 13) epochs. During these dates, the rapid evolution of the system produced complexities in the spectral modeling, due to the presence of an extra jet ejecta component (July 6; Wood et al. 2021), or due to flux variability (July 13). Here we discuss the details of the spectral analyses in both of these epochs.

3.2.1. July 6

The hard-to-soft accretion state transition is associated with the launching of discrete jet ejections (Homan et al. 2020). On 2018 July 6, discrete jet ejections were resolved by very long baseline interferometry imaging (Bright et al. 2020; Wood et al. 2021) of J1820, which motivates fitting an alternative phenomenological model for this epoch. In particular, jet ejections on average produce a steep, optically thin radio to millimeter spectrum. Thus, on this date, we model the emission of jet ejections by including an additional single power law in addition to the broken power law representing the compact jet, since both may be present in the transition state. This component is modeled with pegpwrlw with the photon index fixed at 1.2. We keep the cutoff of both models as indicated in Section 3.1. For this epoch, we extend the prior of the break frequency of the compact jet to be within the frequency range in which the jet ejecta do not dominate, i.e., above (sub)-millimeter. Thus, the spectral break position reported in Table 3 for this epoch corresponds to an upper limit (the higher frequency typically observed in BH XRBs), to reflect our data limitations rather than MCMC constraints from the parameter posterior. To test the need for this additional component, we compare fits with and without this additional single power law in our model. Ultimately these tests revealed that the addition of the jet ejecta component not only better describes our data in this epoch, but also results in spectral indices for the compact jet component that are more consistent with those produced via synchrotron emission ($\alpha_{thick} \approx 0.04$ and $\alpha_{thin} \approx -0.14$ without the extra power law). Thus we favor the addition of the single power-law component to model this epoch. Furthermore, a radio flare detected at 15 GHz, on top of an overall radio emission decline, illustrates the rapid evolution of the jet properties on this epoch (see Extended Data Figure 1 in Bright et al. 2020), while on July 7, observations at 8.4 GHz with the VLBA show no radio core, suggesting that the compact jet had already quenched (Wood et al. 2021). Thus, we caution that as the jet ejecta component dominates the emission at longer wavelengths, and due to the rapid evolution, the compact jet parameters are not as well constrained in this epoch.

3.2.2. July 13

In the broadband spectrum of July 13 (Figure 2, panel (b)) we notice an excess of emission in the IR bands above our best-fit model. Although some of the IR data correspond to 3σ upper limits, we explore different explanations for this possible excess. Some of the IR data used in this epoch are only quasi simultaneous (1–2 days prior) with the other multiwavelength data, thus we suspect that flux variability may be causing this IR excess. Upon comparing the IR data taken in the B10.7 band, we find that the flux density decreases from 4.8 mJy to at least 1.49 mJy over a 24 hr period, confirming our suspicions. Such rapidly variable and fading (over timescales of order hours) IR emission has been observed recently in another BH XRB, MAXI J1535–571 (Baglio et al. 2018b; Russell et al. 2020b), where it also affected broadband spectral modeling efforts. Therefore, given the rapid variability occurring during the period sampled by the July 13 epoch, where the compact jet is rapidly fading between the days sampled, the data presented here likely only represent an average snapshot of the broadband spectrum at this stage of the outburst. Alternatively, evidence of a disk wind present in the soft state (Sánchez-Sierras & Muñoz-Darias 2020) can explain the near-infrared excess. Using X-shooter data from July 13 and 15, Koljonen et al. (2023) modeled the effects of a disk wind/atmosphere in the broadband spectrum (near-infrared/optical, UV, and X-ray) of J1820. They found that the wind/atmosphere sitting above the disk reprocesses the disk's thermal emission into a quasi-thermal near-infrared/optical bump, although their model somewhat underpredicts the data. Other explanations to this potential excess include synchrotron emission from the recently switched off jet (IR excess due to the onset of the jet has been observed in other sources, e.g., Jain et al. 2001; Saikia et al. 2019) and nonthermal emission from a hot inner flow that becomes optically thin in the hard-to-soft state transition (Poutanen et al. 2014), although we stress that the VISIR data on this epoch are not detections, but 3σ upper limits.

4. Discussion

The results of our broadband spectral modeling allow us to observe and connect the spectral changes of J1820 throughout the course of its full outburst. In this section we first describe the spectral parameter evolution and compare to the observed behavior of other sources. Then, we use these results to connect the spectral parameters to jet and accretion flow properties. We include similar analyses of other BH XRBs in the literature and we discuss the implications of our findings.

4.1. Source Evolution

Figure 3 displays the evolution of a selection of parameters over the course of J1820's 2018–2019 outburst. During the rise of the outburst,[61] the synchrotron spectral break moves from the IR into the submillimeter bands[62] ($\approx 10^{14}–10^{12}$ Hz, see panel (a)), accompanied by an increase in the X-ray photon index, suggesting a gradual softening of the X-ray spectrum (panel (b)) over a period of 2 months. Over this period, the best-fit disk temperatures tend to be high compared to those

---

[61] While the actual rise was short and took place in March (see Figure 1), we classify spectral states following Shidatsu et al. (2019) and refer to the outburst rise as the period comprising 2018 March–June.

[62] Due to the sparse data in the IR band, the spectral break evolution can be accounted for with α_{thin} changes.

inferred from the NICER data ($kT_{in} \sim 0.2$ keV; Wang et al. 2020; Dziełak et al. 2021). The disk luminosity is persistently dominated by the corona, with high L_c/L_d values (panel (d)).[63] During the hard state rise, the X-ray spectrum (up to 100 keV) is well described by two Comptonization zones (e.g., Dziełak et al. 2021; Zdziarski et al. 2021; Yang et al. 2022; Kawamura et al. 2023), in which inner and outer corona are responsible for the hard and soft Comptonization components, respectively. However, our Swift/XRT data are limited to 1–10 keV, which probe a small portion of the soft zone only. Including a two-component Comptonization model would result in lower disk temperatures, more consistent with those expected in a truncated disk in the hard state, and explain why our fits lead to higher temperatures. Another possible bias in the disk temperature is the soft excess due to the reflection component, caused by photons from the corona that are reprocessed by the disk. We do not include this component, since it is not resolved in our Swift/XRT spectra. Lastly, during the hard state rise, a hard-to-hard transition has been reported around MJD 58257 ($\approx$May 19), which suggests that J1820 underwent a failed outburst (Stiele & Kong 2020; Wang et al. 2020; Ma et al. 2021). Our sample includes the epoch right before the transition occurred. Thus, we do not observe its effects, and it does not seem to interfere with the subsequent broadband evolution.

As the source evolves into the soft state, the jet spectral break moves below the frequencies that our data sample ($\lesssim 10^8$ Hz), while the X-ray photon index reaches its highest value. We observe a cooling trend in the disk temperature, and the disk dominates the source luminosity, as expected for the soft state.

In the outburst decay, the spectral break frequency gradually increases from the radio, back to the IR bands, while the X-ray spectrum hardens as in the initial phase of the outburst. The disk reaches its coolest temperatures, staying relatively steady at ≈ 0.2 keV. The source luminosity is again dominated by the corona, but with lower luminosities compared to the rise of the outburst.

The other two sources that have displayed similar behavior are MAXI J1836–194 (Russell et al. 2013b, 2014) and MAXI J1535–571 (Russell et al. 2020b, hereafter J1836 and J1535, respectively), although unlike J1820 neither was observed while evolving through all of the typical accretion states in succession. J1836 was observed to evolve from the hard state to the HIMS, after which the X-ray softening stalled, and the source decayed back to the hard state. This spectral evolution took place over the course of $\approx$6 weeks. The source was observed once during its outburst rise (Russell et al. 2014), where the broadband spectrum was characterized by an inverted radio spectrum ($\alpha_{thick} \approx 0.7$), a cool disk ($kT_{disk} \approx 0.23$ keV), and a hard power-law component in the X-rays ($\Gamma \approx 1.73$). Initially, the spectral break was located at $\sim 2.3 \times 10^{11}$ Hz. In the following three observational epochs, J1836 was settled in the HIMS, during which it began to soften but never reached the full soft state. During this state, and over a couple of weeks, the radio spectrum flattened ($\alpha_{thick} \approx 0.2$), and the disk contribution increased as it became hotter ($kT_{disk} \approx 0.42$ keV). The X-ray power law steepened, with a maximum value of $\Gamma \approx 2.03$. Due to sparse data, the spectral break was difficult to constrain in these epochs, but remained in

the $\approx 10^{11}$ Hz range. As the source outburst started to decay, the radio spectrum became inverted again and was relatively steady, while the disk contribution decreased ($kT_{disk} \approx 0.1$ keV), the X-ray spectrum hardened ($\Gamma \approx 1.78$), and the spectral break frequency increased by over 2 orders of magnitude (up to $\approx 5 \times 10^{13}$ Hz) in $\sim$1 month. We observe overall similar behavior in J1820. In particular, we can directly compare the outburst decay phase, in which α_{thick} is consistent with an inverted spectrum, the disk is colder compared to previous epochs, the X-ray component is hard ($\gtrsim 1.6$), and the spectral break frequency increases by a few orders of magnitude. While both sources follow an overall cooling trend, the disk in J1836 became hotter during its softest state in the HIMS, which, based on our fits, we do not observe in J1820, although it is worth noting that Koljonen et al. (2023) found a temperature of $\approx$1 keV on July 13.

For the case of J1535, Russell et al. (2020b) focused on the rise of the outburst, in which the broadband spectrum evolved from the HIMS to the SIMS in a matter of days. During the first five of the six observational epochs the source was in the HIMS. The broadband spectrum was characterized by a flat radio spectrum ($\alpha_{thick} \approx 0.1$), a fairly constant disk temperature ($kT_{disk} \approx 0.2$ keV), a hard X-ray component ($\Gamma = 1.74$–1.95), and a spectral break located at $\approx 10^{13}$ Hz. These properties changed drastically as the source entered into the SIMS: the disk cooled down ($kT_{disk} \approx 0.09$ keV) and the X-ray spectrum softened ($\Gamma \approx 2.17$). More interestingly, the radio spectrum consisted of a single power-law component with a spectral break below 4.5×10^9 Hz. Overall, this is the same behavior we observe in J1820 during the rise of its outburst and transition to the soft state, where our model favors a steep radio spectrum. In both sources there is also evidence of jet ejecta launched during the transition to their softer states. Radio monitoring of J1535 in 2017 December tracked the motion of jet knots launched from the system, and constrained the time of ejections to around the HIMS–SIMS transition (Russell et al. 2019c). In J1820, radio monitoring in early July links the observed radio flaring to the launching of jet ejecta and constrains the ejection time to MJD 58305.60 ± 0.04 (July 6; Wood et al. 2021), which is during the hard-to-soft state transition. The ejection time coincides with a broadband spectrum dominated by a steep optically thin radio component associated with the jet ejecta (see Section 3.2.1), suggesting that the compact jet had already quenched. Although the launching of the ejecta and the compact jet quenching cannot be linked directly due to the low cadence of observations, they likely occur around the same time.

4.2. Mapping Spectral Parameters to Jet Properties

The frequency and flux density of the spectral break are key pieces of information used to infer the properties of the first acceleration zone at the base of the jet. As outlined by Chaty et al. (2011) and following the analyses done for J1836 (Russell et al. 2014) and J1535 (Russell et al. 2020b), and assuming equipartition between particle energy and magnetic field energy density, the frequency and flux density can be used to estimate the radius R_F (or height) and magnetic field B_F of the first acceleration zone:[64]

$$B_F \propto S_{\nu,b}^{-2/(2p+13)} \nu_b, \qquad (1)$$

and:

$$R_\mathrm{F} \propto S_{\nu,\mathrm{b}}^{(p+6)/(2p+13)} \nu_\mathrm{b}^{-1}, \qquad (2)$$

where ν_b is the spectral break frequency, $S_{\nu,\mathrm{b}}$ is the flux density at the spectral break, and p is the power-law index of the electron energy distribution (where $p = 1 - 2\alpha_\mathrm{thin}$). Using our spectral modeling results and Equations (1) and (2), we obtain the evolution of R_F and B_F presented in Figure 4, where errors are calculated using Monte Carlo methods and using the parameter posteriors. The distance from the base of the jet (where particles are first accelerated) to above the BH has been previously estimated from J1820's timing properties. For example, for April 12, Tetarenko et al. (2021) estimated a physical distance[65] of $\approx 10^{12}$ cm and magnetic field strength $> 6 \times 10^3$ G. These estimates are comparable to our result for April 12. Our May 17 estimate is in good agreement with the limit placed for the size scale of the IR-emitting region of $\lesssim 10^{12}$ cm (Markoff et al. 2020) on May 31. We can now compare our results again to the observed evolutions of J1836 and J1535 during similar phases of their outbursts, represented by gray diamonds and triangles, respectively, in Figure 4. When interpreting this figure, note that the timescales of evolution are different for each system, implying a different duration of each state. For the outburst rise in J1535, the radius and magnetic field of the first acceleration zone at the jet base were relatively constant during the HIMS ($R_\mathrm{F} \sim 10^3$–$10^4\ r_\mathrm{g}$ and $B_\mathrm{F} \sim 10^4$ G, respectively). However, in the HIMS–SIMS transition, R_F increased by 3 orders of magnitude while B_F decreased by the same amount over the course of 1 day. The highest value of R_F and lowest value of B_F were found in the SIMS. In the case of J1820, the values at the transition follow the same overall trend. We caution that, for the July 6 data, the flux density and position of the jet break need to be interpreted carefully (see Section 3.2.1). In the soft state, we observe the highest R_F and lowest B_F, consistent with J1535's evolution. For the reversed transition in J1836, R_F was largest during the HIMS ($\sim 10^5$–$10^6\ r_\mathrm{g}$) but receded by ~ 3 orders of magnitude during the declining hard state. Combining these results with measurements of the inner radius of the disk (R_in) from their spectral fits, Russell et al. (2014, 2020b) inferred that particle acceleration must occur at larger scales than R_in. Additionally, the opposite evolutions of ν_b and R_F imply that the jet becomes fainter as particles are accelerated further from the BH and at larger scales, but it recovers as the acceleration point recedes and becomes smaller. In J1820 we see similar behavior during the outburst decay. For the first time we observe the compact jet quenching and recovering throughout the full outburst of a BH XRB. Moreover, its evolution is consistent with that of other sources in similar phases of their outbursts, as shown in Figure 4, where we have included B_F and R_F for BH XRBs and neutron stars (NSs) with spectral break measurements from the literature: 4U 1728-34 (Díaz Trigo et al. 2017), 4U 0614+091 (Migliari et al. 2010), Aql X-1 (Díaz Trigo et al. 2018), XTE J1118+480 (Russell et al. 2013a), 4U 1543-47 (Russell et al. 2013a), XTE J1550-564 (Russell et al. 2013a), GX 339-4

---

[65] We use $1 r_\mathrm{g} \sim 10^6$ cm for J1820.

(Gandhi et al. 2011; Russell et al. 2013a), Cyg X-1 (Russell et al. 2013a), and V404 Cyg (Chandra & Kanekar 2017; Tetarenko et al. 2019). From these sources, only Aql X-1 and V404 Cyg have multiple measurements over the course of their respective outbursts. These results motivate multiwavelength campaigns for future XRBs in outburst (BHs and NSs), to understand better whether this is universal behavior among jet-launching sources.

4.3. Connecting Jet Properties to Accretion Flow Properties

During the rise phase of their outbursts, J1535 and J1820 displayed a rapid broadband spectral evolution. In J1535, the HIMS–SIMS transition was particularly fast, as ν_b shifted by 4 orders of magnitude to lower frequencies over the course of a day, accompanied by a softening X-ray spectrum. The state transition in J1820 spans almost a week, where ν_b moves by at least 3 orders of magnitude in frequency, again with an X-ray softening. During the decay phase the jet recovery in J1820 occurs more gradually, where ν_b shifts back to frequencies comparable to the rising phase over ~ 2 weeks, and the X-ray spectrum hardens. Even more gradual was the jet recovery in J1836, in which ν_b shifted to higher frequencies over the course of a month while the X-ray component hardened. A similar timescale was observed in GX 339-4, in which the jet recovered in about a month, during the transition back to the hard state in the decay of its 2010–2011 outburst (Corbel et al. 2013). This behavior indicates that the jet recovery (ν_b shifting back to higher frequencies) is closely tied to the accretion flow becoming hot and optically thin or "accretion flow recovery" (X-ray hardening). We discuss more direct evidence of these changes and possible implications below.

4.3.1. Soft Comptonization Component

One way to connect the accretion flow properties to the jet properties is to search for correlations between the parameters that dominate their emission. For example, one possible correlation is between ν_b and Γ, which was studied by Koljonen et al. (2015). The relation was determined from observations of BH XRBs and active galactic nuclei (AGN; see Figure 5), including hard X-rays. This comparison can be made for AGN with subarcsecond-resolution, multiwavelength broadband spectra, which allows one to isolate the core emission from the host galaxy. Koljonen et al. (2015) observed that these AGN display a broken power-law, self-absorbed synchrotron spectrum, that is flat/inverted in the optically thick portion, just as in XRBs. When comparing BH XRBs and AGN, it is observed that as ν_b moves to lower frequencies, Γ increases (the spectrum is softer).

One of the sources included in this analysis is J1836, in which Γ follows a clear anticorrelation with jet frequency (see Koljonen et al. 2015, Figure 2). During the HIMS, J1535 also followed this correlation (Russell et al. 2020b). However, as the source softened, ν_b was lower than the expected value for that Γ. In a similar phase of the outburst, the source MAXI J1659–152 (van der Horst et al. 2013) also showed deviations from this correlation. In Figure 5 we show our results for J1820. Several of our measurements are in good agreement with the correlation observed for the other sources displayed in the figure, suggesting similarity in the mechanism governing these changes among sources. However, some exceptions are the data from, October 6, 11, 14, and 19, where

the ν_b estimates are less constrained in our fits. While in these cases the values do not confirm the correlation, they certainly encompass part of the area predicted by it. We also caution that for both J1535 and J1820, the Γ measurements are obtained from X-ray spectra covering up to 10 keV, while Koljonen et al. (2015) included much higher energies.

4.3.2. Reverberation Lags

The origin of the hard X-ray emission in BH XRBs is typically attributed to a corona of hot electrons, although its geometry and physical properties remain unclear. For simplicity, it is sometimes treated as a lamppost, where the corona is situated above the accretion disk, but it could also be an extended region comprising the inner part of the accretion disk. Extensive work has been done in studying J1820's timing properties to understand the structure of the corona. In this section, we discuss these studies and connect them to our findings from broadband phenomenological modeling.

Regardless of the coronal geometry, a fraction of the hard X-ray photons may be intercepted and reprocessed by the disk, producing a soft component in the X-ray spectrum. The disk–corona separation provides key observational evidence to probe the changing coronal geometry, since a larger separation would cause the soft X-ray photons to reach the observer with a delay with respect to the hard ones. This delay is known as reverberation lag, and could allow us to connect the corona to the jet observed in the HIMS.

J1820 was observed by NICER beginning the day following its discovery (Uttley et al. 2018), providing a complete data set to observe reverberation lags as the source evolved through the outburst. Using this technique, Kara et al. (2019) reported reverberation lags corresponding to the rising hard state, and found that soft lags progressively move toward shorter timescales (i.e., probing a progressively smaller emitting region) and constant iron emission line profile, suggesting that the corona contracts over time. They proposed an initially vertically extended corona with a compact core that becomes more compact as the source evolves through the rising hard state. In addition, they found that the reverberation lag becomes longer during the state transition in J1820 (De Marco et al. 2021; Wang et al. 2021), probing an increasingly more extended emitting region. Later, Wang et al. (2022) systematically searched for reverberation lags in BH XRBs (and candidates) in the NICER archive, and found that this is generic behavior. Their search also included later stages of the outburst, including the transition to the soft state. Using the Hard X-ray Modulation Telescope (HXMT), Wang et al. (2020) reported lags in the hard state rise as well. The time lags observed in the same frequency range as in Kara et al. (2019) are harder and larger, implying a disk–corona separation of $\sim 1000 r_g$, as opposed to the $\sim 10 r_g$ in Kara et al. (2019). They also found a correlation between high-frequency lags and photon index of hard X-ray emission. They interpreted this result as two regions where the hard X-rays are emitted. One of them is the compact corona suggested in the aforementioned works, and the other is a large-scale jet where energetic electrons up-scatter soft photons from the disk (see also Espinasse et al. 2020). Other BH XRBs present evidence of two Comptonization regions based on timing properties: interference of disk and synchrotron Comptonization emission at different radii, applied to

GX 339-4 and XTE J1748-288 (Veledina 2016), corona and compact jet in GRS 1915+105 (García et al. 2022), and the dual-corona model of GX 339-4 (Peirano et al. 2023).

As we emphasize in Section 4.1, our limited X-ray coverage hinders the possibility to constrain different Comptonization components. However, because we track the evolution of the spectral break, and consequently, R_F, we consider it more appropriate to compare to Kara et al. (2019) and subsequent works. Their findings suggest that the corona could correspond to the base of the jet, as proposed originally in Markoff et al. (2005), which vertically expands and launches the jet ejecta in the intermediate states, although a potential connection to the compact jet component was not thoroughly explored. Particularly in J1820, the coronal expansion precedes the radio flaring activity (Bright et al. 2018) linked to the launching of jet ejecta (Wood et al. 2021), further supporting this scenario.

In Figure 4, bottom panel, we observe how the location of the first acceleration zone increases during the rising hard state, with its highest value in the soft state. As discussed previously in Section 4.2, J1535 displays the same behavior during the HIMS–SIMS transition. For the case of J1836, Lucchini et al. (2021) studied its behavior during the hard–HIMS transition, finding a strong correlation between the initial jet radius and power spectral hue, which characterizes the shape of the power-law spectrum (whether it is flat or peaked). The correlation showed that as the jet base radius increased in size, the hard X-ray spectrum softened and became more peaked (this trend has also been observed in other sources; Cao et al. 2022). Since one way to soften the Comptonization spectrum is by decreasing the optical depth of the emitting region, they interpreted this result as an expanding jet base during the state transition, a scenario consistent with Wang et al. (2022) and our results. Figure 6, top panel, compares the evolution of the jet spectral break with the evolution of the soft X-ray lags up to the onset of the outburst decay (Wang J., private communication). The details of this data set can be found in Wang et al. (2022). The increasing timescale of lags between the rising hard and intermediate states suggests that we are probing an emitting region that is increasing in size. This coincides with ν_b moving to lower frequencies (base of the jet moving away) and an increasing R_F (expanding jet base). The opposite evolution in the soft-to-hard state transition indicates a smaller emitting region, consistent with recovery of the compact jet. This clear trend strongly argues for a scenario where the corona corresponds to the jet base region.

4.3.3. Quasi-periodic Oscillations

The X-ray emission in BH XRBs can display variability features at certain frequencies, which are known as quasi-periodic oscillations (QPOs; e.g., Ingram & Motta 2019). Depending on their frequency, QPOs can be broadly classified as low-frequency QPOs (LFQPOs; $\sim 10^{-2}$–10 Hz), typically observed in the hard state and HIMS, and high-frequency QPOs (~ 10–10^3 Hz), characteristic of the soft state. The changing frequency of QPOs is closely related to changes in the geometry of the accretion flow, since both the frequency and inner radius of the disk change during the course of an outburst. The origin of LFQPOs is still debated, but it is typically attributed to instabilities in the accretion flow, instabilities in the jet (Ferreira et al. 2022), or Lense–Thirring

precession of either the inner hot accretion flow present in the hard state (Stella & Vietri 1998; Ingram et al. 2009), which is directly related to the Compton tail in the X-ray spectrum, or of a small-scale jet (Ma et al. 2021). In J1820 only LFQPOs have been reported throughout the outburst (e.g., Stiele & Kong 2020, with Swift-XRT and NICER data), as shown in Figure 6, top panel. In the rising hard state, the QPO frequencies remain $\lesssim 1$ Hz, suggesting a larger radial extent of the inner accretion flow during this period (Ingram et al. 2009). In the state transition, the QPO frequency increases remarkably fast (on timescales similar to the jet spectral break), suggesting a small extent to the inner accretion flow during this phase. When J1820 transitions back to the (declining) hard state, the QPO frequency falls again to $\lesssim 2$ Hz, consistent with the inner disk radius receding and being replaced by a radially extended hot inner flow.

Insight/HXMT has played an important role in the detection of LFQPOs. Particularly in the hard state rise, the properties of LFQPOs discovered above 30 keV can be explained by the precession of a small-scale jet (Ma et al. 2021). In this model, a small-scale jet precesses above the disk, producing LFQPOs at different energies: high-energy LFQPOs come from the jet base while low-energy LFQPOs from the top, where cooling becomes important. This model seems to explain well the LFQPO properties observed in J1820 (as well as the QPOs observed in the optical band; Thomas et al. 2022), particularly if the jet is located a few r_g above the BH (lamppost geometry) and if its height decreases over the rising hard state period (consistent with the picture proposed in Kara et al. 2019). The magnetic field can accelerate the small-scale jet into a relativistic, large-scale jet, producing broadband synchrotron emission. Later, Ma et al. (2023b) extended this model to include lower-energy ($<$1 keV) LFQPOs from NICER data, and found that the jet and inner disk ring precess together. Our broadband observations and location of the first acceleration zone at the base of the jet support the presence of a relativistic jet that dominates the spectrum throughout the hard state, as expected from this model. More recently, Ma et al. (2023a) focused on a NICER observation on July 6, i.e., the state transition, and proposed a dual-corona model to explain the observed QPO evolution. The model consists of a horizontally expanded corona that envelops the inner region of the accretion disk, with a compact corona inside the inner edge. During the transition, the compact corona remains unchanged while the other vertically expands and is associated with the ejecta on this epoch.

While we cannot directly link the QPO frequencies to the spectral break frequencies (due to a lack of data of the soft state and variability in the declining hard state), they seem to evolve in the opposite way, suggesting that changes in the jet are connected to changes in the geometry of the accretion flow. An analysis of QPOs in the source GRS 1915+105 was able to establish such connection, coupling the corona and launching of the jet (Méndez et al. 2022). The study revealed that, as the QPO frequency decreases below $\lesssim 2$ Hz, the corona becomes less radially extended and more vertically extended until the compact jet is launched. This study shows that QPOs are another key piece of information that can be used to understand the corona–jet connection better, and highlights the importance of combining this technique with multiwavelength spectral

modeling and reverberation lags to create the most complete picture of the physical processes at play in BH XRBs.

5. Conclusions

We present the results of a quasi-simultaneous, multi-wavelength observing campaign of the BH XRB J1820 over the course of its 2018–2019 outburst. This campaign allowed us to observe, for the first time, the full evolution of a BH XRB as it transitions through the different spectral states, with the potential to provide new insights into the behavior of the compact jet and its connection to the contemporaneous changes in the accretion flow. We collect the most complete data set spanning from radio through X-rays, which we compile into 19 single epochs, encompassing 7 months of the outburst. We fit the broadband spectrum of each observational epoch with a phenomenological model that accounts for interstellar absorption and extinction, a persistent compact jet, discrete jet ejecta (when applicable), the accretion flow, and the companion star. Our findings can be summarized as follows:

1. The broadband evolution of J1820 is consistent with that observed for other BH XRBs. In particular, we observe the jet spectral break shift to lower frequencies as the jet emission fades in the soft state, and move back to IR frequencies as the system returns to the hard state, indicating that the compact jet has recovered.

2. Tracking the jet spectral break and flux density at its location allows us to place estimates on the distance to the first acceleration zone at the base of the jet (R_F) and the magnetic field strength (B_F) in this region. These measurements have been conducted for only two other sources while evolving through spectral states: J1836 and J1535. The behavior of J1820 in corresponding phases of the outbursts is consistent with both. When combining these results with other XRBs with jet spectral break measurements, we observe similar evolutions and values of B_F and R_F among all sources. Moreover, the R_F evolution distinctly shows the change in the jet base location during the state changes, indicating the quenching and recovery of the compact jet.

3. Measurements of the jet spectral break and X-ray photon index in BH XRBs (including J1820) and AGN seem to follow a negative correlation, indicating a connection between inflow and outflow. The fact that several accreting systems at different scales follow this anticorrelation strongly suggests similarity in the mechanism governing these changes among accreting sources.

4. The evolving jet activity observed in J1820 appears to be related with X-ray timing properties (reverberation lags). This trend points toward the scenario where the corona is thought to be at the base of the jet.

Our findings further motivate the need for high-cadence monitoring of BH XRBs in outburst, to obtain well-sampled broadband spectra and to characterize the broadband evolution. This will help to constrain the jet spectrum better, which in turn will allow us to understand the complex connection between the jet and the accretion flow better. In this context, next-generation telescopes will play a key role in following up transient systems. The James Webb Space telescope instruments now make it possible to observe the spectral

break when positioned through the mid-infrared bands (1.1×10^{13}–5×10^{14} Hz), which is essential to track the jet base, where particle acceleration begins, and its evolution. The Vera C. Rubin Observatory will provide wide-area coverage of the optical sky, enabling rapid detection of optical transients. Since BH XRBs in outburst tend to brighten first in the optical, real-time alerts will allow us to improve out multiwavelength campaigns to follow up these objects. Finally, timing and polarimetry techniques in the submillimeter region are already providing valuable insight into jet physics (see the results from the PITCH-BLACK Survey[66]). The combined capabilities of current and next-generation telescopes when monitoring future BH XRBs in outburst, together with the ongoing development of relativistic jet simulations, foresees a promising future for the jet physics field.

Facility: AMI, VLA, ALMA, NOEMA, SMA, JCMT, VLT (VISIR, XSHOOTER), REM, LCO, Swift (XRT and UVOT), and AAVSO.

Software: CASA (McMullin et al. 2007), GILDAS (http://www.iram.fr/IRAMFR/GILDAS), STARLINK (Currie et al. 2014), ESOREFLEX (Freudling et al. 2013), AQUA (Testa et al. 2004), DAOPHOT (Stetson 1987), HEASOFT (Nasa High Energy Astrophysics Science Archive Research Center (Heasarc) 2014), XSPEC (Arnaud 1996), and FTOOLS (Blackburn 1995).

Appendix A
Markov Chain Monte Carlo Convergence

Figure 7 presents a sample posterior distribution from our MCMC runs, corresponding to April 12. These posterior distributions are used to determine the best-fit parameters, as well as the convergence of each parameter.
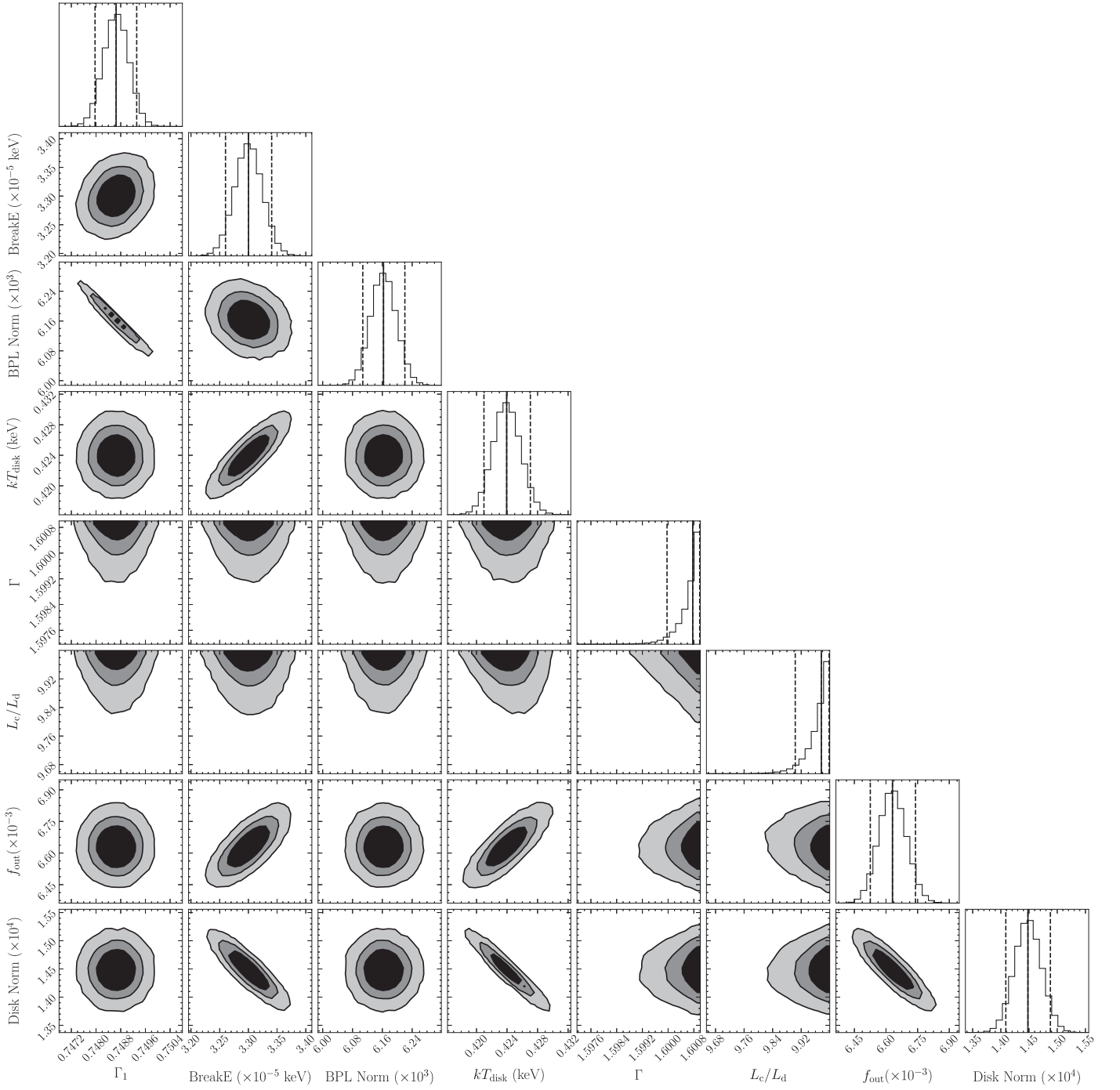
Figure 7. The one- and two-dimensional MCMC posterior distributions of the parameters in the spectral fitting of the April 12 data. The black, dark gray, and light gray regions correspond to the 68%, 90%, and 99% credible intervals, respectively. The solid line in the middle of the one-dimensional posterior distributions represents the median value, while the left and right dashed lines represent the 16% and 84% percentiles, respectively. Note that in the Γ and $L_{\rm c}/L_{\rm d}$ parameters the upper limit is unconstrained, since it is consistent with the hard limit of the model.

Appendix B
Spectral Modeling

In this section, we present additional material pertaining to the spectral modeling results. Figure 8 displays a sample spectrum corresponding to data obtained on April 12, with each individual component contributing to the broadband emission in our phenomenological model. Table 4 summarizes the spectral break frequencies and flux densities at the spectral break, resulting from our spectral modeling. Figure 9 shows the residuals obtained from the spectral fits presented in Section 3.1.
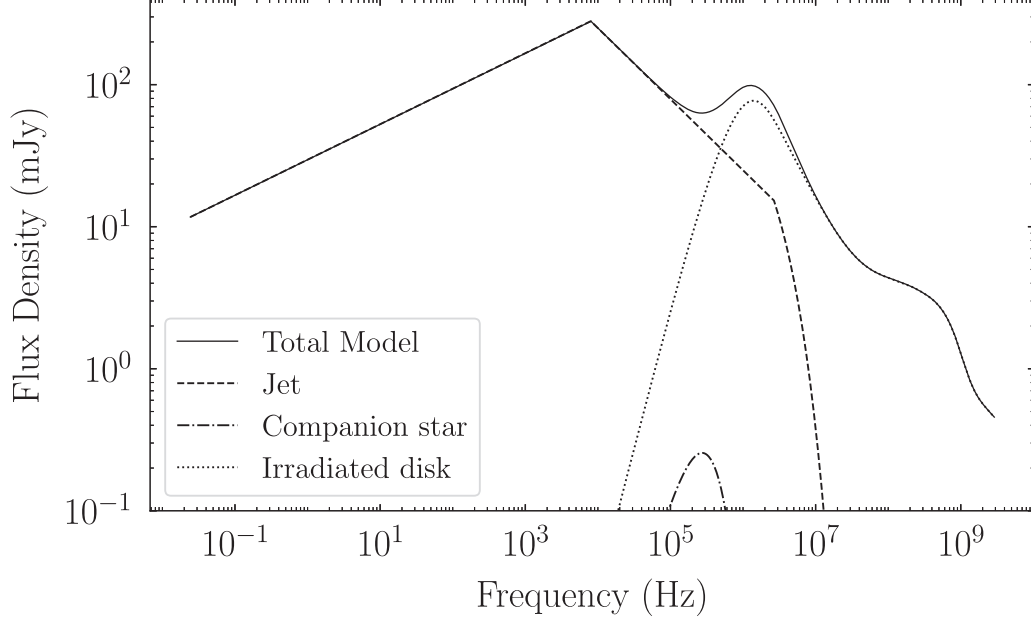
Figure 8. A sample broadband spectrum corresponding to data obtained on April 12, displaying the contribution of each component to the emission.
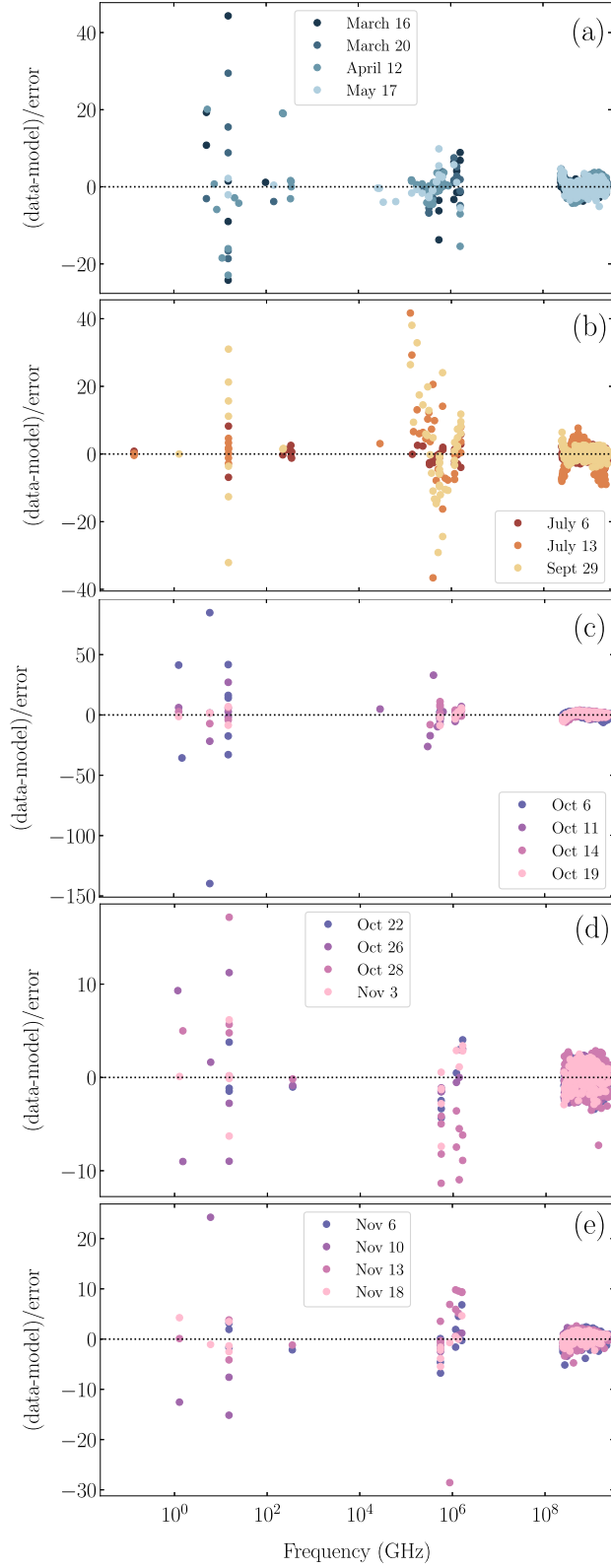
Figure 9. Fit residuals, defined as (data − model)/error, corresponding to the broadband spectral fits presented in Figure 2. Panel (a) displays the model residuals corresponding to the rising hard state (blue). Panel (b) shows the model residuals of the intermediate (July 6 and September 29) and soft (July 13) states (yellow). Panels (c), (d), and (e) show the residuals corresponding to the declining hard state (pink). Note that the color codes for the accretion states are matched in Figures 1, 2, 3, 4, and 6.

Appendix C
Observations

Tables 5, 6, and 7 detail the Swift/UVOT and Swift/XRT observations presented in this work.

Table 5
Summary of the Swift/UVOT Observations of MAXI J1820+070

Obs. ID	Date		U	V	UVOT Filter UVW1	UVM2	UVW2
00010627005	2018-03-16 03:01:32	Exposure	⋯	⋯	183.8	276.3	393.4
		Count rate	⋯	⋯	176.9	97.7	187.4
00010627009	2018-03-20 18:37:18	Exposure	⋯	⋯	189.7	285.2	390.6
		Count rate	⋯	⋯	254.8	148.1	267.1
00088657004	2018-05-17 21:43:10	Exposure	⋯	⋯	177.9	368.2	357.1
		Count rate	⋯	⋯	137.7	73.3	132
00010754001	2018-07-06 15:24:07	Exposure	⋯	⋯	316.7	597.9	634.6
		Count rate	⋯	⋯	125.7	67.4	121.9
00010754004	2018-07-13 08:15:03	Exposure	⋯	⋯	269.5	481.7	540.1
		Count rate	⋯	⋯	154.3	81.6	152.3
00010627102	2018-09-29 07:38:22	Exposure	⋯	95.24	189.7	285.2	379.7
		Count rate	⋯	25.4	42.86	23.1	42.8
00010627109	2018-10-06 02:15:36	Exposure	⋯	⋯	176.9	265.5	⋯
		Count rate	⋯	⋯	33.1	17.6	⋯
00010627111	2018-10-11 06:41:03	Exposure	⋯	⋯	102.1	152.3	203.5
		Count rate	⋯	⋯	46.3	23	40.8
00010627113	2018-10-15 17:34:08	Exposure	⋯	⋯	163.2	244.8	326.5
		Count rate	⋯	⋯	38.7	20.1	35
00010627115	2018-10-19 07:12:57	Exposure	⋯	113.9	227.1	341.4	455.5
		Count rate	⋯	27.9	37.2	19	34.4
00010627116	2018-10-21 00:42:47	Exposure	⋯	⋯	100.2	364.4	561.7
		Count rate	⋯	⋯	34.3	18.5	33.4
00010627119	2018-10-26 11:27:29	Exposure	⋯	137.6	275.4	414.1	551.9
		Count rate	⋯	21.2	28.1	14.4	27.2
00010627120	2018-10-28 14:33:23	Exposure	⋯	48.98	97.21	146.4	195.6
		Count rate	⋯	22.4	28.9	14.3	25.1
00010627123	2018-11-03 10:55:07	Exposure	⋯	69.66	140.5	210.4	280.3
		Count rate	⋯	15	22.7	10.8	19.6
00010627125	2018-11-06 04:07:05	Exposure	⋯	102.1	203.5	305.9	407.2
		Count rate	⋯	14.8	19	10.3	18.3
00010627127	2018-11-10 13:11:47	Exposure	⋯	34.23	68.67	103.1	137.6
		Count rate	⋯	12.1	15.7	7.7	13.2
00010627128	2018-11-12 08:29:53	Exposure	⋯	120.8	241	362	483
		Count rate	⋯	10.3	13.8	7.1	11.5
00010627131	2018-11-18 04:26:15	Exposure	153.7	145.4	291.1	436.8	582.5
		Count rate	19.3	7.2	8.8	4.2	8.2

Note. These observations are simultaneous to the XRT data used in this work, while additional nonsimultaneous UV observations can be found in Table 6. The exposure times are measured in seconds, while the units of the count rates are counts s^{-1}.

(This table is available in machine-readable form.)

Table 6
Summary of the Swift/UVOT Observations of MAXI J1820+070

Obs. ID	Date		U	V	UVOT Filter UVW1	UVM2	UVW2
00010627001	2018-03-14 20:54:55	Exposure	...	...	219.3	329.5	345.4
		Count rate	...	...	161.5	85.8	156.1
00010627006	2018-03-17 02:52:57	Exposure	...	...	203.5	305.9	408.6
		Count rate	...	...	199.9	104.2	196.9
00010627008	2018-03-19 18:40:57	Exposure	...	...	195.6	294	359.1
		Count rate	...	...	257.3	145.3	248.2
00010627010	2018-03-21 18:45:57	Exposure	...	...	210.4	315.7	426.7
		Count rate	...	...	295.8	157.2	284.4
00010627030	2018-04-11 05:25:57	Exposure	...	...	...	...	1134
		Count rate	...	...	...	...	261.2
00010627037	2018-04-14 06:45:57	Exposure	...	...	...	...	959
		Count rate	...	...	...	...	227.4
00010627076	2018-07-08 05:36:57	Exposure	...	...	112	183.2	224.1
		Count rate	...	...	114.0	62	114.7
00010627079	2018-07-08 23:19:57	Exposure	...	...	92.3	151.6	184.8
		Count rate	...	...	116.1	58.1	98.8
00010627083	2018-07-11 21:35:44	Exposure	...	...	175	297.7	285.2
		Count rate	...	...	135.2	77.5	138.1
00010754002	2018-07-11 03:34:09	Exposure	...	...	417.1	...	158.2
		Count rate	...	...	132.1	...	128.6
00088657008	2018-07-15 19:41:48	Exposure	...	...	218.4	...	...
		Count rate	...	...	151.6	...	...
00010627104	2018-09-30 10:43:57	Exposure	...	90.3	180.9	355.7	362
		Count rate	...	23	40.1	21.4	41.3
00010627105	2018-10-01 13:49:57	Exposure	...	87.4	175	370.7	349.2
		Count rate	...	22.7	38.8	21.5	39.1
00088657010	2018-09-27 22:00:57	Exposure	...	83.4	167.1	249.8	333.4
		Count rate	...	28.1	45.7	25	45.8
00010627110	2018-10-09 00:13:57	Exposure	...	50	100.2	150.4	200.5
		Count rate	...	28.7	37.9	19.8	37.5
00010627112	2018-10-13 06:13:57	Exposure	...	...	186.8	280.3	373.8
		Count rate	...	...	43.7	22.3	38.9
00010627114	2018-10-17 05:48:56	Exposure	...	...	170.1	341.4	339.3
		Count rate	...	...	40.4	19	35.7
00088657011	2018-10-30 00:04:57	Exposure	...	102.1	205.5	450.7	411.2
		Count rate	...	19.5	26.9	13.2	24.2
00010627124	2018-11-04 15:25:57	Exposure	...	110.1	...	...	582.5
		Count rate	...	17.2	...	...	19.7
00010627126	2018-11-08 16:41:57	Exposure	...	69.7	139.5	208.4	278.3
		Count rate	...	12.1	17.2	9.3	15.2
00010627129	2018-11-14 12:42:34	Exposure	90.1	114.9	231.1	346.2	461.4
		Count rate	28	9.591	12.1	6	11.5

Note. These are not simultaneous to the XRT exposures used in this work. The exposure times are measured in seconds, while the units of the count rates are counts s^{-1}.

(This table is available in machine-readable form.)

Table 7
Summary of the Swift/XRT Observations of MAXI J1820+070

Obs. ID	Date	Exposure (s)	Count Rate (s^{-1})	Pileup Corrected?
00010627005	2018-03-16 03:01:32	978.1	48.15	Yes
00010627009	2018-03-20 18:37:18	991.5	131.9	Yes
00010627034	2018-04-12 06:58:53	1018	100.4	Yes
00010627035	2018-04-12 10:11:03	888.3	102.5	Yes
00088657004	2018-05-17 21:43:10	777.4	123.7	Yes
00010754001	2018-07-06 15:24:07	1994.9	110.7	Yes
00010754004	2018-07-13 08:15:03	1607	119	Yes
00010627102	2018-09-29 07:38:22	1108	115.8	Yes
00010627109	2018-10-06 02:15:36	1037	86.6	No
00010627111	2018-10-11 06:41:03	588.8	25.4	No
00010627113	2018-10-15 17:34:08	943	13.9	No
00010627115	2018-10-19 07:17:24	1348	10.3	No
00010627116	2018-10-21 00:42:47	1732	7.7	No
00010627119	2018-10-26 11:27:29	448.1	5.1	No
00010627120	2018-10-28 14:33:23	12508.1	3.9	No
00010627123	2018-11-03 10:55:07	1386	2.7	No
00010627125	2018-11-06 04:07:05	2197	2.2	No
00010627127	2018-11-10 13:11:47	399.1	1.4	No
00010627128	2018-11-12 08:29:53	2014	1.1	No
00010627131	2018-11-18 04:26:15	1657	0.6	No

(This table is available in machine-readable form.)

Appendix D
Summary of Flux Densities

Tables 8, 9, 10, and 11 summarize the radio, IR/optical, and UV flux densities and frequencies utilized in this work to construct each broadband spectrum.

Table 8
Flux Densities of MAXI J1820+070 at Radio and Submillimeter Frequencies

Telescope	Date (2018)	MJD	Frequency (GHz)	Flux Density (mJy)	Reference
AMI-LA	Mar 14	58191	15	17.32 ± 0.15	...
AMI-LA	Mar 15	58192	15	21.53 ± 0.42	...
eMERLIN	Mar 16	58193	5.07	23.2 ± 0.4	(2)
AMI-LA	Mar 16	58193	15	32.18 ± 0.25	...
VLBA	Mar 16	58193	15	20.01 ± 0.10	(9)
NOEMA	Mar 16	58193	97	30 ± 3	(8)
eMERLIN	Mar 17	58194	5.07	26.6 ± 0.4	(2)
AMI-LA	Mar 18	58195	15	50.65 ± 0.30	...
AMI-LA	Mar 19	58196	15	52.08 ± 0.19	...
AMI-LA	Mar 20	58197	15	58.44 ± 0.31	...
NOEMA	Mar 20	58197	146	80.8 ± 8.0	(8)
AMI-LA	Mar 21	58198	15	60.46 ± 0.31	...
eMERLIN	Mar 22	58199	5.07	38 ± 1	(2)
AMI-LA	Mar 22	58199	15	66.96 ± 0.38	...
AMI-LA	Apr 11	58219	15	47.48 ± 0.43	...
VLA	Apr 12	58220	5.3	46.0 ± 0.1	(5)
VLA	Apr 12	58220	7.5	48.1 ± 0.2	(5)
VLA	Apr 12	58220	8.5	48.3 ± 0.2	(5)
VLA	Apr 12	58220	11.1	49.2 ± 0.2	(5)
VLA	Apr 12	58220	20.7	58.7 ± 1.1	(5)
VLA	Apr 12	58220	25.5	60.5 ± 1.1	(5)
SMA	Apr 12	58220	226.6	151.1 ± 2.0	(6)
SMA	Apr 12	58220	234.6	166.9 ± 2.8	(6)
ALMA	Apr 12	58220	336.6	124.4 ± 0.07	(4)
ALMA	Apr 12	58220	338.6	124.9 ± 0.06	(4)
ALMA	Apr 12	58220	348.6	125.8 ± 0.06	(4)
ALMA	Apr 12	58220	350.4	125.9 ± 0.06	(4)
AMI-LA	Apr 13	58221	15	48.65 ± 0.54	...

Note. A portion of this table is shown here for guidance regarding its form and content.

References. (1) Broderick et al. (2018); (2) Bright et al. (2020); (3) Shaw et al. (2021; project code: 18A–277); (4) project code: 2017.1.01103.T; (5) project code: 18A–470; (6) project codes: 2018A-S011 and 2017B-S010; (7) project code: M18BP025; (8) project codes: W17BM and W17BN; and (9) Atri et al. (2020).

(This table is available in its entirety in machine-readable form.)

Table 9
Flux Densities of MAXI J1820+070 at Infrared and Optical Frequencies

Facility	Band	Date (2018)	MJD	Wavelength (μm)	Frequency (GHz)	Flux Density (mJy)	Reference
AAVSO	V	Mar 14	58191	0.55	5.5×10^5	24.27 ± 0.10	(1)
AAVSO	V	Mar 15	58192	0.55	5.5×10^5	23.98 ± 2.25	(1)
AAVSO	V	Mar 16	58193	0.55	5.5×10^5	28.50 ± 2.69	(1)
AAVSO	V	Mar 17	58194	0.55	5.5×10^5	38.60 ± 3.80	(1)
AAVSO	V	Mar 18	58195	0.55	5.5×10^5	36.05 ± 3.81	(1)
AAVSO	V	Mar 19	58196	0.55	5.5×10^5	34.80 ± 3.59	(1)
AAVSO	V	Mar 20	58197	0.55	5.5×10^5	36.77 ± 2.89	(1)
AAVSO	V	Mar 21	58198	0.55	5.5×10^5	41.18 ± 3.85	(1)
REM	K	Mar 22	58199	2.13	1.41×10^5	119.23 ± 12.34	(2)
REM	H	Mar 22	58199	1.64	1.83×10^5	91.51 ± 26.10	(2)
REM	J	Mar 22	58199	1.25	2.40×10^5	70.36 ± 5.72	(2)
REM	z	Mar 22	58199	0.89	3.36×10^5	32.22 ± 3.61	(2)
REM	z	Mar 22	58199	0.89	3.36×10^5	32.21 ± 3.53	(2)
REM	z	Mar 22	58199	0.89	3.36×10^5	33.12 ± 4.21	(2)
REM	i	Mar 22	58199	0.75	4.02×10^5	34.68 ± 4.64	(2)
REM	i	Mar 22	58199	0.75	4.02×10^5	34.81 ± 4.45	(2)
REM	i	Mar 22	58199	0.75	4.02×10^5	35.71 ± 4.37	(2)
REM	r	Mar 22	58199	0.61	4.88×10^5	40.29 ± 4.552	(2)
REM	r	Mar 22	58199	0.61	4.88×10^5	39.79 ± 5.07	(2)
REM	r	Mar 22	58199	0.61	4.88×10^5	40.78 ± 4.99	(2)
REM	g	Mar 22	58199	0.47	6.42×10^5	47.98 ± 3.61	(2)
REM	g	Mar 22	58199	0.47	6.42×10^5	46.44 ± 4.72	(2)
REM	g	Mar 22	58199	0.47	6.42×10^5	48.10 ± 4.43	(2)

Note. A portion of this table is shown here for guidance regarding its form and content.
References. (1) Kafka (2021) and (2) proposal code 37025.

(This table is available in its entirety in machine-readable form.)

Table 10
Flux Densities of MAXI J1820+070 at Optical Frequencies from the X-shooter Instrument (Project Code: 0101.D-0356)

Date (2018)	Wavelength (μm)	Frequency (GHz)	Flux Density (mJy)
April 12	2.14	1.40×10^5	83.19 ± 5.25
	1.61	1.87×10^5	64.18 ± 4.61
	0.99	3.01×10^5	50.83 ± 0.13
	0.94	3.19×10^5	50.40 ± 0.38
	0.87	3.38×10^5	48.66 ± 0.45
	0.83	3.60×10^5	48.27 ± 0.14
	0.78	3.85×10^5	47.38 ± 0.26
	0.72	4.14×10^5	46.80 ± 0.37
	0.67	4.47×10^5	46.0 ± 0.29
	0.62	4.87×10^5	45.49 ± 0.04
	0.56	5.34×10^5	44.44 ± 0.38
	0.50	5.98×10^5	43.64 ± 0.16
	0.45	6.70×10^5	43.20 ± 0.36
	0.39	7.62×10^5	41.26 ± 0.65
	0.35	8.55×10^5	40.63 ± 0.02
July 13	2.32	1.29×10^5	10.31 ± 0.12
	2.14	1.40×10^5	10.83 ± 0.15
	1.99	1.51×10^5	11.86 ± 0.68
	1.66	1.81×10^5	13.54 ± 0.31
	1.49	2.01×10^5	15.51 ± 0.72
	1.24	2.42×10^5	17.29 ± 0.50
	1.07	2.79×10^5	19.15 ± 0.55
	0.97	3.08×10^5	20.32 ± 0.19
	0.92	3.26×10^5	21.02 ± 0.14
	0.86	3.47×10^5	21.61 ± 0.35
	0.81	3.72×10^5	22.72 ± 0.21
	0.75	3.99×10^5	23.13 ± 0.05
	0.70	4.31×10^5	23.27 ± 0.05
	0.64	4.69×10^5	23.39 ± 0.03
	0.58	5.16×10^5	23.15 ± 0.28
	0.52	5.77×10^5	22.56 ± 0.37
	0.46	6.47×10^5	22.01 ± 0.37
	0.41	7.36×10^5	21.15 ± 0.26
	0.36	8.39×10^5	20.67 ± 0.19
September 29	2.32	1.29×10^5	43.41 ± 0.08
	2.14	1.40×10^5	46.23 ± 0.06
	1.99	1.51×10^5	49.39 ± 0.24
	1.66	1.81×10^5	54.32 ± 0.06
	1.49	2.01×10^5	58.43 ± 0.11
	1.24	2.42×10^5	62.04 ± 0.09
	1.07	2.79×10^5	65.11 ± 0.14
	0.97	3.08×10^5	67.43 ± 0.03
	0.92	3.26×10^5	68.34 ± 0.03
	0.86	3.47×10^5	67.79 ± 0.05
	0.81	3.72×10^5	69.22 ± 0.02
	0.75	3.99×10^5	68.41 ± 0.03
	0.70	4.31×10^5	67.03 ± 0.05
	0.64	4.69×10^5	65.24 ± 0.07
	0.58	5.16×10^5	62.98 ± 0.05
	0.52	5.77×10^5	60.53 ± 0.14
	0.46	6.47×10^5	57.13 ± 0.07
	0.41	7.36×10^5	53.23 ± 0.15
	0.36	8.39×10^5	48.50 ± 0.15

Note. The original date of the observation included in the representative epoch July 13 is 2018 July 14.

(This table is available in machine-readable form.)

Table 11
Flux Densities of MAXI J1820+070 at UV Frequencies

Band	Date (2018)	MJD	Wavelength (μm)	Frequency (GHz)	Flux Density (mJy)
UW1	Mar 14	58191	0.26	1.16×10^6	15.2 ± 0.6
UM2	Mar 14	58191	0.22	1.34×10^6	12.0 ± 0.3
UW2	Mar 14	58191	0.20	1.48×10^6	12.9 ± 0.4
UW1	Mar 16	58193	0.26	1.16×10^6	16.7 ± 0.6
UM2	Mar 16	58193	0.22	1.34×10^6	13.7 ± 0.3
UW2	Mar 16	58193	0.20	1.48×10^6	15.4 ± 0.4
UW1	Mar 17	58194	0.26	1.16×10^6	18.8 ± 0.7
UM2	Mar 17	58194	0.22	1.34×10^6	14.6 ± 0.3
UW2	Mar 17	58194	0.20	1.48×10^6	16.2 ± 0.5
UW1	Mar 19	58196	0.26	1.16×10^6	24.3 ± 0.9
UM2	Mar 19	58196	0.22	1.34×10^6	20.3 ± 0.5
UW2	Mar 19	58196	0.20	1.48×10^6	20.4 ± 0.6
UW1	Mar 20	58197	0.26	1.16×10^6	24 ± 0.9
UM2	Mar 20	58197	0.22	1.34×10^6	20.7 ± 0.5
UW2	Mar 20	58197	0.20	1.48×10^6	22 ± 0.7
UW1	Mar 21	58198	0.26	1.16×10^6	27.9 ± 1.1
UM2	Mar 21	58198	0.22	1.34×10^6	22 ± 0.5
UW2	Mar 21	58198	0.20	1.48×10^6	23.4 ± 0.7

Note. A portion of this table is shown here for guidance regarding its form and content.

(This table is available in its entirety in machine-readable form.)

ORCID iDs

Constanza Echiburú-Trujillo ● https://orcid.org/0000-0001-8436-1847
Alexandra J. Tetarenko ● https://orcid.org/0000-0003-3906-4354
Daryl Haggard ● https://orcid.org/0000-0001-6803-2138
Thomas D. Russell ● https://orcid.org/0000-0002-7930-2276
Karri I. I. Koljonen ● https://orcid.org/0000-0002-9677-1533
Arash Bahramian ● https://orcid.org/0000-0003-2506-6041
Jingyi Wang ● https://orcid.org/0000-0002-1742-2125
Joe Bright ● https://orcid.org/0000-0002-7735-5796
David M. Russell ● https://orcid.org/0000-0002-3500-631X
Diego Altamirano ● https://orcid.org/0000-0002-3422-0074
M. Cristina Baglio ● https://orcid.org/0000-0003-1285-4057
Chiara Ceccobello ● https://orcid.org/0000-0002-4767-9925
Maria Diaz Trigo ● https://orcid.org/0000-0001-7796-4279
Dipankar Maitra ● https://orcid.org/0000-0003-1897-6872
Aldrin Gabuya ● https://orcid.org/0000-0003-1541-7557
Elena Gallo ● https://orcid.org/0000-0001-5802-6041
Jeroen Homan ● https://orcid.org/0000-0001-8371-2713
Erin Kara ● https://orcid.org/0000-0003-0172-0854
Matteo Lucchini ● https://orcid.org/0000-0002-2235-3347
Sera Markoff ● https://orcid.org/0000-0001-9564-0876
James C. A. Miller-Jones ● https://orcid.org/0000-0003-3124-2814
Jerome Rodriguez ● https://orcid.org/0000-0002-4151-4468
Payaswini Saikia ● https://orcid.org/0000-0002-5319-6620
Craig L. Sarazin ● https://orcid.org/0000-0003-0167-0981
Tariq Shahbaz ● https://orcid.org/0000-0003-1331-5442
Gregory Sivakoff ● https://orcid.org/0000-0001-6682-916X
Roberto Soria ● https://orcid.org/0000-0002-4622-796X
Vincenzo Testa ● https://orcid.org/0000-0003-1033-1340
Bailey E. Tetarenko ● https://orcid.org/0000-0003-2636-6644

References

Adachi, R., Murata, K. L., Oeda, M., et al. 2020, ATel, 13502, 1
Arnaud, K. A. 1996, in ASP Conf. Ser. 101, Astronomical Data Analysis Software and Systems V, ed. G. H. Jacoby & J. Barnes (San Francisco, CA: ASP), 17
Atri, P., Miller-Jones, J. C. A., Bahramian, A., et al. 2020, MNRAS, 493, L81
Baglio, M. C., Homan, J., Russell, D. M., et al. 2021a, ATel, 14582, 1
Baglio, M. C., Russell, D., Qaissieh, T. A., et al. 2018a, ATel, 12128, 1
Baglio, M. C., Russell, D. M., Alabarta, K., et al. 2023, ATel, 16192, 1
Baglio, M. C., Russell, D. M., Casella, P., et al. 2018b, ApJ, 867, 114
Baglio, M. C., Russell, D. M., & Lewis, F. 2018c, ATel, 11418, 1
Baglio, M. C., Russell, D. M., Qaissieh, T. A., et al. 2019, ATel, 12596, 1
Baglio, M. C., Russell, D. M., Saikia, P., Bramich, D. M., & Lewis, F. 2021b, ATel, 14492, 1
Bahramian, A., Motta, S., Atri, P., & Miller-Jones, J. 2019, ATel, 12573, 1
Belloni, T. M., Motta, S. E., & Muñoz-Darias, T. 2011, BASI, 39, 409
Bharali, P., Chauhan, J., & Boruah, K. 2019, MNRAS, 487, 5946
Blackburn, J. K. 1995, in ASP Conf. Ser. 77, Astronomical Data Analysis Software and Systems IV, ed. R. A. Shaw, H. E. Payne, & J. J. E. Hayes, 367
Bramich, D. M., & Freudling, W. 2012, MNRAS, 424, 1584
Breeveld, A. A., Curran, P. A., Hoversten, E. A., et al. 2010, MNRAS, 406, 1687
Bright, J., Motta, S., Fender, R., Perrott, Y., & Titterington, D. 2018, ATel, 11827, 1
Bright, J., Motta, S., Williams, D., et al. 2019, ATel, 13041, 1
Bright, J. S., Fender, R. P., Motta, S. E., et al. 2020, NatAs, 4, 697
Broderick, J., Russell, T., Bright, J., et al. 2018, ATel, 11887, 1
Cangemi, F., Rodriguez, J., Belloni, T., et al. 2023, A&A, 669, A65
Cao, Z., Lucchini, M., Markoff, S., Connors, R. M. T., & Grinberg, V. 2022, MNRAS, 509, 2517
Cardelli, J. A., Clayton, G. C., & Mathis, J. S. 1989, ApJ, 345, 245
Carotenuto, F., Corbel, S., Tremou, E., et al. 2021, MNRAS, 504, 444
Carotenuto, F., Fender, R., Woudt, P., & Miller-Jones, J. 2022, ATel, 15277, 1
Casella, P., Maccarone, T. J., O'Brien, K., et al. 2010, MNRAS, 404, L21
Casella, P., & Pe'er, A. 2009, ApJL, 703, L63
Casella, P., Testa, V., Russell, D. M., Belloni, T. M., & Maccarone, T. J. 2018, ATel, 11833, 1
Ceccobello, C., Cavecchi, Y., Heemskerk, M. H. M., et al. 2018, MNRAS, 473, 4417
Chakraborty, S., Navale, N., Ratheesh, A., & Bhattacharyya, S. 2020, MNRAS, 498, 5873
Chandra, P., & Kanekar, N. 2017, ApJ, 846, 111
Chapin, E. L., Berry, D. S., Gibb, A. G., et al. 2013, MNRAS, 430, 2545
Chaty, S., Dubus, G., & Raichoor, A. 2011, A&A, 529, A3
Corbel, S., Aussel, H., Broderick, J. W., et al. 2013, MNRAS, 431, L107
Corbel, S., & Fender, R. P. 2002, ApJL, 573, L35
Corbel, S., Fender, R. P., Tomsick, J. A., Tzioumis, A. K., & Tingay, S. 2004, ApJ, 617, 1272
Corbel, S., Fender, R. P., Tzioumis, A. K., et al. 2002, Sci, 298, 196
Covino, S., Stefanon, M., Sciuto, G., et al. 2004, Proc. SPIE, 5492, 1622
Currie, M. J., Berry, D. S., Jenness, T., et al. 2014, in ASP Conf. Ser. 485, Astronomical Data Analysis Software and Systems XXIII, ed. N. Manset & P. Forshay (San Francisco, CA: ASP), 391
De Marco, B., Zdziarski, A. A., Ponti, G., et al. 2021, A&A, 654, A14
Dempsey, J. T., Friberg, P., Jenness, T., et al. 2013, MNRAS, 430, 2534
Díaz Trigo, M., Altamirano, D., Dinçer, T., et al. 2018, A&A, 616, A23
Díaz Trigo, M., Migliari, S., Miller-Jones, J. C. A., et al. 2017, A&A, 600, A8
Dobrzycka, D., Momany, Y., Lundin, L., et al. 2012, Proc. SPIE, 8448, 84481P
Done, C., Gierliński, M., & Kubota, A. 2007, A&ARv, 15, 1
Dziełak, M. A., De Marco, B., & Zdziarski, A. A. 2021, MNRAS, 506, 2020
Espinasse, M., Corbel, S., Kaaret, P., et al. 2020, ApJL, 895, L31
Fender, R. 2006, Compact Stellar X-Ray Sources, Vol. 39 (Cambridge: Cambridge Univ. Press), 381
Fender, R. P., Belloni, T. M., & Gallo, E. 2004, MNRAS, 355, 1105
Fender, R. P., Homan, J., & Belloni, T. M. 2009, MNRAS, 396, 1370
Ferreira, J., Marcel, G., Petrucci, P. O., et al. 2022, A&A, 660, A66
Fordham, J. L. A., Moorhead, C. F., & Galbraith, R. F. 2000, MNRAS, 312, 83
Freudling, W., Romaniello, M., Bramich, D. M., et al. 2013, A&A, 559, A96
Gandhi, P., Blain, A. W., Russell, D. M., et al. 2011, ApJL, 740, L13
García, F., Karpouzas, K., Méndez, M., et al. 2022, MNRAS, 513, 4196
Geweke, J. 1992, in Bayesian Statistics 4, ed. J. M. Bernardo & M. H. DeGroot (Oxford: Oxford Univ. Press), 169
Gierliński, M., Done, C., & Page, K. 2008, MNRAS, 388, 753
Gierliński, M., Done, C., & Page, K. 2009, MNRAS, 392, 1106

Gilfanov, M. 2010, in The Jet Paradigm, Lecture Notes in Physics Vol. 794, ed. T. Belloni (Berlin: Springer), 17

Goodman, J., & Weare, J. 2010, Commun. Appl. Math. Comput. Sci., 5, 65

Goodwin, A. J., Russell, D. M., Galloway, D. K., et al. 2020, MNRAS, 498, 3429

Hambsch, J., Ulowetz, J., Vanmunster, T., Cejudo, D., & Patterson, J. 2019, ATel, 13014, 1

Heinz, S., & Sunyaev, R. A. 2003, MNRAS, 343, L59

Henden, A. A., Levine, S. E., Terrell, D., Smith, T. C., & Welch, D. 2012, JAVSO, 40, 430

Hickish, J., Razavi-Ghods, N., Perrott, Y. C., et al. 2018, MNRAS, 475, 5677

Holland, W. S., Bintley, D., Chapin, E. L., et al. 2013, MNRAS, 430, 2513

Homan, J., Baglio, M. C., Saikia, P., et al. 2023, ATel, 16200, 1

Homan, J., & Belloni, T. 2005, Ap&SS, 300, 107

Homan, J., Bright, J., Motta, S. E., et al. 2020, ApJL, 891, L29

Homan, J., Stevens, A. L., Altamirano, D., et al. 2018a, ATel, 12068, 1

Homan, J., Uttley, P., Gendreau, K., et al. 2018b, ATel, 11820, 1

Ingram, A., Done, C., & Fragile, P. C. 2009, MNRAS, 397, L101

Ingram, A. R., & Motta, S. E. 2019, NewAR, 85, 101524

Jain, R. K., Bailyn, C. D., Orosz, J. A., McClintock, J. E., & Remillard, R. A. 2001, ApJL, 554, L181

Jamil, O., Fender, R. P., & Kaiser, C. R. 2010, MNRAS, 401, 394

Jonker, P. G., & Nelemans, G. 2004, MNRAS, 354, 355

Jordi, K., Grebel, E. K., & Ammon, K. 2006, A&A, 460, 339

Kafka, S. 2021, Observations from the AAVSO International Database, https://www.aavso.org/

Kalemci, E., Dinçer, T., Tomsick, J. A., et al. 2013, ApJ, 779, 95

Kara, E., Steiner, J. F., Fabian, A. C., et al. 2019, Natur, 565, 198

Kausch, W., Noll, S., Smette, A., et al. 2015, A&A, 576, A78

Kawamura, T., Done, C., Axelsson, M., & Takahashi, T. 2023, MNRAS, 519, 4434

Kawamuro, T., Negoro, H., Yoneyama, T., et al. 2018, ATel, 11399, 1

Kochanek, C. S., Shappee, B. J., Stanek, K. Z., et al. 2017, PASP, 129, 104502

Koljonen, K. I. I., Long, K. S., Matthews, J. H., & Knigge, C. 2023, MNRAS, 521, 4190

Koljonen, K. I. I., Russell, D. M., Fernández-Ontiveros, J. A., et al. 2015, ApJ, 814, 139

Krimm, H. A., Holland, S. T., Corbet, R. H. D., et al. 2013, ApJS, 209, 14

Lagage, P. O., Pel, J. W., Authier, M., et al. 2004, Msngr, 117, 12

Lewis, F. 2018, RTSRE, 1, 237

Lewis, F., Russell, D. M., Fender, R. P., Roche, P., & Clark, J. S. 2008, arXiv:0811.2336

Lucchini, M., Russell, T. D., Markoff, S. B., et al. 2021, MNRAS, 501, 5910

Ma, R., Méndez, M., García, F., et al. 2023a, MNRAS, 525, 854

Ma, X., Tao, L., Zhang, S.-N., et al. 2021, NatAs, 5, 94

Ma, X., Zhang, L., Tao, L., et al. 2023b, ApJ, 948, 116

Maccarone, T. J. 2003, A&A, 409, 697

Mairs, S., Dempsey, J. T., Bell, G. S., et al. 2021, AJ, 162, 191

Malzac, J. 2013, MNRAS, 429, L20

Malzac, J. 2014, MNRAS, 443, 299

Malzac, J., Dumont, A. M., & Mouchet, M. 2005, A&A, 430, 761

Marino, A., Barnier, S., Petrucci, P. O., et al. 2021, A&A, 656, A63

Markoff, S. 2010, in The Jet Paradigm, Lecture Notes in Physics Vol. 794, ed. T. Belloni (Berlin: Springer), 143

Markoff, S., Falcke, H., & Fender, R. 2001, A&A, 372, L25

Markoff, S., Nowak, M. A., & Wilms, J. 2005, ApJ, 635, 1203

Markoff, S., Russell, D. M., Dexter, J., et al. 2020, MNRAS, 495, 525

Matsuoka, M., Kawasaki, K., Ueno, S., et al. 2009, PASJ, 61, 999

McCully, C., Volgenau, N. H., Harbeck, D.-R., et al. 2018, Proc. SPIE, 10707, 107070K

McMullin, J. P., Waters, B., Schiebel, D., Young, W., & Golap, K. 2007, in ASP Conf. Ser. 376, Astronomical Data Analysis Software and Systems XVI, ed. R. A. Shaw, F. Hill, & D. J. Bell (San Francisco, CA: ASP), 127

Méndez, M., Karpouzas, K., García, F., et al. 2022, NatAs, 6, 577

Migliari, S., Tomsick, J. A., Miller-Jones, J. C. A., et al. 2010, ApJ, 710, 117

Mihara, T., Nakajima, M., Sugizaki, M., et al. 2011, PASJ, 63, S623

Miller-Jones, J. C. A., Fender, R. P., & Nakar, E. 2006, MNRAS, 367, 1432

Miller-Jones, J. C. A., Sivakoff, G. R., Altamirano, D., et al. 2012, MNRAS, 421, 468

Molinari, E., Covino, S., Crimi, G., et al. 2014, Proc. SPIE, 9147, 91476X

Motta, S. E., Bright, J., & Fender, R. 2018, ATel, 12064, 1

Nasa High Energy Astrophysics Science Archive Research Center (Heasarc), 2014 HEAsoft: Unified Release of FTOOLS and XANADU, Astrophysics Source Code Library, ascl:1408.004

Özbey Arabacı, M., Kalemci, E., Dinçer, T., et al. 2022, MNRAS, 514, 3894

Paice, J. A., Gandhi, P., Shahbaz, T., et al. 2019, MNRAS, 490, L62

Paice, J. A., Gandhi, P., Shahbaz, T., et al. 2021, MNRAS, 505, 3452

Peirano, V., Méndez, M., García, F., & Belloni, T. 2023, MNRAS, 519, 1336

Pirbhoy, S. F., Baglio, M. C., Russell, D. M., et al. 2020, ATel, 13451, 1

Polko, P., Meier, D. L., & Markoff, S. 2014, MNRAS, 438, 959

Poutanen, J., Veledina, A., & Revnivtsev, M. G. 2014, MNRAS, 445, 3987

Prabhakar, G., Mandal, S., Athulya, M. P., & Nandi, A. 2022, MNRAS, 514, 6102

Rodi, J., Tramacere, A., Onori, F., et al. 2021, ApJ, 910, 21

Rodriguez, J., Corbel, S., & Tomsick, J. A. 2003, ApJ, 595, 1032

Rodriguez, J., Shaw, S. E., Hannikainen, D. C., et al. 2008, ApJ, 675, 1449

Romano, P., Campana, S., Chincarini, G., et al. 2006, A&A, 456, 917

Romero, G. E., Boettcher, M., Markoff, S., & Tavecchio, F. 2017, SSRv, 207, 5

Roques, J.-P., & Jourdain, E. 2019, ApJ, 870, 92

Russell, D. M., Baglio, M. C., Bright, J., et al. 2018, ATel, 11533, 1

Russell, D. M., Baglio, M. C., & Lewis, F. 2019a, ATel, 12534, 1

Russell, D. M., Bramich, D. M., Lewis, F., et al. 2019b, AN, 340, 278

Russell, D. M., Casella, P., Kalemci, E., et al. 2020, MNRAS, 495, 182

Russell, D. M., Markoff, S., Casella, P., et al. 2013a, MNRAS, 429, 815

Russell, D. M., Russell, T. D., Miller-Jones, J. C. A., et al. 2013b, ApJL, 768, L35

Russell, T. D., Lucchini, M., Tetarenko, A. J., et al. 2020b, MNRAS, 498, 5772

Russell, T. D., Soria, R., Miller-Jones, J. C. A., et al. 2014, MNRAS, 439, 1390

Russell, T. D., Tetarenko, A. J., Miller-Jones, J. C. A., et al. 2019c, ApJ, 883, 198

Rybicki, G. B., & Lightman, A. P. 1979, Radiative Processes in Astrophysics (New York: Wiley)

Saikia, P., Russell, D. M., Bramich, D. M., et al. 2019, ApJ, 887, 21

Sánchez-Sierras, J., & Muñoz-Darias, T. 2020, A&A, 640, L3

Sasaki, R., Negoro, H., Nakahira, S., et al. 2020, ATel, 13530, 1

Shakura, N. I., & Sunyaev, R. A. 1973, A&A, 500, 33

Shappee, B. J., Prieto, J. L., Grupe, D., et al. 2014, ApJ, 788, 48

Shaw, A. W., Plotkin, R. M., Miller-Jones, J. C. A., et al. 2021, ApJ, 907, 34

Shidatsu, M., Nakahira, S., Murata, K. L., et al. 2019, ApJ, 874, 183

Shidatsu, M., Nakahira, S., Yamada, S., et al. 2018, ApJ, 868, 54

Smette, A., Sana, H., Noll, S., et al. 2015, A&A, 576, A77

Stella, L., & Vietri, M. 1998, ApJL, 492, L59

Stetson, P. B. 1987, PASP, 99, 191

Stetson, P. B. 1990, PASP, 102, 932

Stiele, H., & Kong, A. K. H. 2020, ApJ, 889, 142

Testa, V., Antonelli, L. A., Di Paola, A., et al. 2004, Proc. SPIE, 5496, 729

Tetarenko, A. J., Casella, P., Miller-Jones, J. C. A., et al. 2021, MNRAS, 504, 3862

Tetarenko, A. J., Petitpas, G., Sivakoff, G. R., et al. 2018, ATel, 11831, 1

Tetarenko, A. J., Sivakoff, G. R., Miller-Jones, J. C. A., et al. 2015, ApJ, 805, 30

Tetarenko, A. J., Sivakoff, G. R., Miller-Jones, J. C. A., et al. 2017, MNRAS, 469, 3141

Tetarenko, A. J., Sivakoff, G. R., Miller-Jones, J. C. A., et al. 2019, MNRAS, 482, 2950

Tetarenko, B. E., Sivakoff, G. R., Heinke, C. O., & Gladstone, J. C. 2016, ApJS, 222, 15

Thomas, J. K., Buckley, D. A. H., Charles, P. A., et al. 2022, MNRAS, 513, L35

Tonry, J. L., Denneau, L., Flewelling, H., et al. 2018, ApJ, 867, 105

Torres, M. A. P., Casares, J., Jiménez-Ibarra, F., et al. 2019, ApJL, 882, L21

Torres, M. A. P., Casares, J., Jiménez-Ibarra, F., et al. 2020, ApJL, 893, L37

Tucker, M. A., Shappee, B. J., Holoien, T. W. S., et al. 2018, ApJL, 867, L9

Ulowetz, J., Myers, G., & Patterson, J. 2019, ATel, 12567, 1

Uttley, P., Gendreau, K., Markwardt, C., et al. 2018, ATel, 11423, 1

Vadawale, S. V., Rao, A. R., Naik, S., et al. 2003, ApJ, 597, 1023

van der Horst, A. J., Curran, P. A., Miller-Jones, J. C. A., et al. 2013, MNRAS, 436, 2625

Veledina, A. 2016, ApJ, 832, 181

Vernet, J., Dekker, H., D'Odorico, S., et al. 2011, A&A, 536, A105

Vitali, F., Zerbi, F. M., Chincarini, G., et al. 2003, Proc. SPIE, 4841, 627

Wang, J., Kara, E., Lucchini, M., et al. 2022, ApJ, 930, 18

Wang, J., Mastroserio, G., Kara, E., et al. 2021, ApJL, 910, L3

Wang, Y., Ji, L., Zhang, S. N., et al. 2020, ApJ, 896, 33
Williams, D., Motta, S., Bright, J., et al. 2019, ATel, 12577, 1
Wilms, J., Allen, A., & McCray, R. 2000, ApJ, 542, 914
Wood, C. M., Miller-Jones, J. C. A., Homan, J., et al. 2021, MNRAS, 505, 3393
Xu, Y., Harrison, F., & Tomsick, J. 2019, ATel, 13025, 1
Yang, Z.-X., Zhang, L., Bu, Q.-C., et al. 2022, ApJ, 932, 7
You, B., Tuo, Y., Li, C., et al. 2021, NatCo, 12, 1025
Zdziarski, A. A., Dziełak, M. A., De Marco, B., Szanecki, M., & Niedźwiecki, A. 2021, ApJL, 909, L9
Zwart, J. T. L., Barker, R. W., Biddulph, P., et al. 2008, MNRAS, 391, 1545